EarthArXiv Cover Sheet

Title: Plio-Pleistocene evolution of westerly moisture transport into the northern tropical Andes

Authors:
David Fastovich
dfastovi@syr.edu, www.davidfastovich.com
Department of Earth and Environmental Sciences, Syracuse University, Syracuse, NY, USA
ORCID ID: 0000-0002-0340-9819

Tripti Bhattacharya
Department of Earth and Environmental Sciences, Syracuse University, Syracuse, NY, USA
ORCID ID: 0000-0002-5528-3760

Lina C. Pérez-Ángel
Institute at Brown for Environment and Society, Department of Earth, Environment and Planetary Sciences, Brown University, Providence, RI, USA
ORCID ID: 0000-0002-2920-7967

Natalie J. Burls
Department of Atmospheric, Oceanic, and Earth Sciences, George Mason University, Fairfax, VA, USA
ORCID ID: 0000-0002-6950-3808

Ran Feng
Department of Earth Sciences, University of Connecticut, University of Connecticut, Storrs, CT, USA

Scott Knapp
Department of Atmospheric, Oceanic, and Earth Sciences, George Mason University, Fairfax, VA, USA
ORCID ID: 0000-0002-9539-2937

Theodor Mayer
Department of Earth Sciences, University of Connecticut, University of Connecticut, Storrs, CT, USA

This preprint is under review at *Earth and Planetary Science Letters* and is not peer reviewed.

Plio-Pleistocene evolution of westerly moisture transport into the northern tropical Andes

David Fastovich[a,*], Tripti Bhattacharya[a], Lina C. Pérez-Ángel[b], Natalie J. Burls[c], Ran Feng[d], Scott Knapp[c], Theodor Mayer[d]

[a]*Department of Earth and Environmental Sciences, Syracuse University, Syracuse, NY, USA*
[b]*Institute at Brown for Environment and Society, Brown University, Provide, RI, USA*
[c]*Department of Atmospheric, Oceanic, and Earth Sciences, George Mason University, Fairfax, VA, USA*
[d]*Department of Earth Sciences, University of Connecticut, University of Connecticut, Storrs, CT, USA*

Abstract

Westerly winds from the eastern equatorial Pacific direct moisture into the Western Cordillera of the northern tropical Andes, where subsequent orographic lifting creates the wettest regions in the world. The Choco low-level jet is emblematic of broader westerly winds in this region and is projected to weaken by the end of the 21st century, but climate models show considerable disagreement about the extent of weakening. Using contemporary observations, we demonstrate that the configuration of westerly winds in the eastern equatorial Pacific is reflected by hydrogen isotopes in precipitation (δD_p) in Ecuador. As westerly winds strengthen, δD_p increases from greater transport of enriched δD_{vapor} from the Eastern Pacific Warm Pool. We apply this framework to a new record of reconstructed δD_p using leaf waxes in ocean sediments off the coast of Ecuador (ODP1239, 0°40.32′ S, 82°4.86′ W) that span the Plio-Pleistocene. Low δD_p in the early Pliocene indicates weak westerly water vapor transport in a warmer climate state, which is attributed to a low sea surface temperature gradient between the cold tongue and off-equatorial regions in the eastern equatorial Pacific. Near the end-Pliocene (˜3 Ma), westerly water vapor transport weakens, possibly from shifts in the Intertropical Convergence Zone, forced by high latitude Northern Hemi-

*Corresponding Author
Email address: dfastovi@syr.edu (David Fastovich)

sphere cooling. In complementary isotope-enabled climate simulations, a weak Choco jet and westerly water vapor transport in the early Pliocene are matched by a decrease in δD_p and hydroclimate changes in the northern tropical Andes. Precipitation from the Choco jet can cause deadly landslides and weakened westerly winds in the early Pliocene implies a southward shift of these hazards along the Pacific coast of the northern tropical Andes in the future.

Keywords:
leaf waxes, isotopes of precipitation, Pliocene, hydroclimate, South America

1. Introduction

The Western Cordillera of the northern tropical Andes contains some of the wettest regions in the world (Poveda and Mesa, 2000) supporting high biodiversity (Rangel et al., 2018; Myers et al., 2000). Interannual changes in precipitation can yield droughts (Vicente-Serrano et al., 2017) and floods (Waylen and Caviedes, 1986). During flood events, high rainfall and extreme topography create ideal conditions for mass wasting. Fatal landslides are common in the northern tropical Andes and have caused thousands of fatalities in the last century that disproportionally impact vulnerable populations (Garcia-Delgado et al., 2022). Increases in regional precipitation amount and seasonality are expected in the coming century (Ramirez-Villegas et al., 2012; Vuille et al., 2008) and threaten to increase the prevalence of landslides, which have accelerated in the last 20 years (Garcia-Delgado et al., 2022). However, accurate projections of precipitation-related risks are hampered by uncertain climate projections (Sierra et al., 2021).

Hydroclimate along the Western Cordillera of the northern tropical Andes is tightly linked to westerly transport from the eastern equatorial Pacific that is largely concentrated in the Choco low-level jet (Hoyos et al., 2018; Poveda et al., 2006; Poveda and Mesa, 2000; Sierra et al., 2021). The westerly Choco jet forms from Coriolis acceleration on tropical southerly winds that cross the equator following the position of the Intertropical Convergence Zone (ITCZ, Poveda and Mesa, 2000; Xie and Philander, 1994). Westerly winds are lofted by tropical easterlies and orographic lifting by the Western Cordillera of the Andes facilitating deep convection and intense precipitation (Poveda and Mesa, 2000). Accordingly, a poor representation of the Choco jet in models produces poor simulations of precipitation for the historic pe-

riod (Sierra et al., 2015). From a synthesis of 26 coupled general circulation models from the Coupled Model Intercomparison Project Phase 5 (CMIP5), more than half cannot capture key characteristics of the Choco jet in historic simulations, such as the intensity or jet core location (Sierra et al., 2018). Poor simulations of the Choco jet are primarily caused by biases in the position of the ITCZ, temperature and pressure gradient biases in the eastern equatorial Pacific, and the representation of topography (Sierra et al., 2018, 2021). This highlights a need to improve our fundamental understanding of atmospheric circulation and moisture transport in this region.

Various paleoclimatic reconstructions suggest that westerly water vapor transport into the northern tropical Andes is sensitive to the background climate. For instance, the Choco jet responds to the equatorial to off-equatorial gradient in sea surface temperature and mean sea level pressure in the eastern tropical Pacific (Poveda and Mesa, 2000; Sierra et al., 2021). During the Last Glacial Maximum, the sea surface temperature gradient across the Equatorial Front in the eastern equatorial Pacific was greater and may have supported a stronger Choco jet (Martínez et al., 2003). Climate simulations of the Little Ice Age demonstrate a similar relationship, linking an intensification of the Choco jet to a greater mean sea level pressure gradient between the eastern equatorial Pacific and the northern tropical Andes (Sierra et al., 2021). It is unclear how changes in westerly transport in this region may be influenced by large-scale reorganizations of sea surface temperature gradients in the Pliocene, a recent geologic epoch with atmospheric carbon dioxide concentrations similar to contemporary levels (Martínez-Botí et al., 2015). The Pliocene is marked by high sea surface temperatures and low sea surface temperature gradients (meridional and zonal) throughout the Pacific (Tierney et al., 2019). Similar to the Pliocene, contemporary El Niño events also produce a low meridional sea surface temperature gradient in the eastern tropical Pacific from warming in the cold tongue. In response to this reduced sea surface temperature gradient, westerly water vapor transport weakens (Poveda et al., 2006), drying the Pacific coast of Colombia, while increasing precipitation in northern Peru (Hoyos et al., 2019) and the Ecuadorian lowlands (Morán-Tejeda et al., 2016). Unfortunately, few paleoclimatic records span the Pliocene in the northern tropical Andes (Etourneau et al., 2010; Grimmer et al., 2018, 2020; Herbert et al., 2016; Lawrence et al., 2006; Seki et al., 2012) and only one examines large scale atmospheric circulation (Hovan, 1995), but it is unclear how regional atmospheric circulation is reflected in existing records. This gap in proxy reconstructions precludes constraining

changes to westerly moisture transport in the eastern equatorial Pacific in warm climates forced by high greenhouse gas concentrations. These uncertainties can be constrained through hydroclimate reconstructions during the Pliocene.

To address this uncertainty, we reconstruct regional atmospheric circulation in the northern tropical Andes through the Plio-Pleistocene. Climate across the Plio-Pleistocene includes global and regional climate changes; notably, the initiation of major Northern Hemisphere glaciation and long term cooling of the eastern equatorial Pacific cold tongue (Lawrence et al., 2006; Liu et al., 2019; Raymo, 1994; Tierney et al., 2019; Wara et al., 2005). By investigating this interval, we aim to constrain the sensitivities of atmospheric circulation in the northern tropical Andes to various forcings using leaf wax biomarkers which track water isotopes in precipitation. Water isotopes in precipitation have been instrumental in reconstructing past hydroclimate and circulation (Bhattacharya et al., 2022; Dee et al., 2023). Applying this approach in the northern tropical Andes is complicated by the dynamic surface uplift of the Andes, which was episodic over the last 80 to 70 Ma. From 15 Ma to the present, the subduction of the Carnegie Ridge has caused exhumation rates in the Western Cordillera of the Andes to increase (Margirier et al., 2023; Spikings et al., 2001, 2010; Spikings and Simpson, 2014; Villagómez and Spikings, 2013). The surface uplift of the Western Cordillera may have left an imprint on precipitation isotopes through Rayleigh distillation, where precipitation isotopes become more depleted as elevation increases and temperature decreases (Rowley and Garzione, 2007). Therefore, disentangling signals of surface uplift and atmospheric circulation in this region is challenging (Pérez-Angel et al., 2022). We address the influence of elevation change on precipitation isotopes by analyzing the contemporary relationship between precipitation isotopes, elevation, and the Choco jet from the Global Network of Isotopes in Precipitation (GNIP) (Aggarwal et al., 2007) along the Western Cordillera of the Andes. Using the interpretive framework offered by this observational data, we present a new record of reconstructed precipitation isotopes ($\delta \mathrm{D}_p$) from ODP1239 (Mix et al., 2003), positioned off the coast of Ecuador. We extracted and measured the hydrogen and carbon isotopic composition of leaf wax biomarkers to track the configuration of westerly water vapor transport during the Plio-Pleistocene. The relative proportion of $H^2 : H^1$ in leaf waxes ($\delta \mathrm{D}_{wax}$) is sensitive to the hydrogen isotopic composition of meteoric waters ($\delta \mathrm{D}_p$) (Sachse et al., 2012). Consequently, $\delta \mathrm{D}_{wax}$ at ODP1239 captures variations in the intensity of westerly water

vapor transport from the Eastern Pacific Warm Pool. Our findings identify a gradual increase in water vapor transport through the Plio-Pleistocene controlled by evolving mechanisms.

2. Methods

2.1. Contemporary δD_p from GNIP

We develop an interpretive framework for understanding variations in reconstructed δD_p through the Plio-Pleistocene using instrumental observations of water isotopes in precipitation from GNIP (Aggarwal et al., 2007). We retrieved all GNIP station data available in Ecuador using the Water Isotope System for Data Analysis, Visualization, and Electronic Retrieval in February 2023 (https://www.iaea.org/resources/nucleus-information-resources). GNIP station data was filtered to retain observations that contained measurements of δD_p and precipitation amount. We applied an additional filter and retained stations with at least 12 consecutive observations (i.e. one year) to minimize the influence of precipitation seasonality (Pérez-Angel et al., 2022). Several stations, like the Quito-Inamhi station, contained more than 12 consecutive observations. For these stations, we take the first $\lfloor \frac{N}{12} \rfloor \times 12$ observations, where N is the number of consecutive observations. For example, the Quito-Inamhi station had 26 months of continuous measurements from 4/1/2011 to 5/31/2013, of which we discarded the last two observations resulting in 24 consecutive observations. By discarding the two observations, we prevent adding observations, and bias, to the wet season. We averaged measured δD_p for long-term monthly means weighted by precipitation amount. Weighting by precipitation amount reduces the influence of months with little precipitation but anomalous measured δD_p.

We model the relationship between the Choco jet index, monthly precipitation, and monthly precipitation-weighted δD_p with a series of linear mixed-effects models. We focus on the Choco jet in these analyses because its westerly transport into western Colombia is demonstrative of broader westerly water vapor transport into the northern tropical Andes (Figure 1F). The Choco jet is well correlated with westerly winds in the eastern equatorial Pacific across several pressure levels (Figure S2). In these linear mixed-effects models, Choco jet intensity and monthly precipitation are fixed effects, elevation is a random effect, and δD_p is the response variable. We perform model selection by comparing all combinations of predictors and corresponding model diagnostics (e.g. Akaike's Information Criterion

and log-likelihood). We also assess linear mixed-effects models where δD_p is cube-root transformed to more evenly weigh high and low elevation stations. High-elevation stations have larger changes in monthly δD_p and contribute more variability to the linear mixed-effects models. Conclusions from linear mixed-effects models with transformed and untransformed monthly δD_p are identical, so for simplicity, we present the untransformed results with all results in Table S1.

2.2. ODP Core 1239A

ODP1239 (0°40.32′ S, 82°4.86′ W) was cored in 2002 and is located ˜120 km off the western coast of Ecuador, on the Carnegie Ridge at 1414 m water depth. The Pliocene portion of the sediments are predominantly pelagic and composed of olive gray nanofossil oozes with varying proportions of clay, diatoms, foraminifers, and micrite (Mix et al., 2003). The South Pacific Subtropical High creates southerly winds along the coast of Peru and Ecuador imparting easterly wind stress, upwelling the Equatorial Undercurrent, and developing the characteristic eastern equatorial Pacific cold tongue (Strub et al., 1998). The extent of the cold tongue is greatest at the end of the austral winter and exposes ODP1239 to cool, nutrient-rich waters (Strub et al., 1998; Locarnini et al., 2013). This oceanographic setting changed very minimally during the Pliocene as ODP1239 migrated eastward alongside the Nazca plate towards Ecuador (Mix et al., 2003). From 6 Ma to present, ODP1239 migrated 2° (˜200 km) eastward and 0.75° (˜75 km) northward suggesting that leaf waxes sourced from Ecuador for the duration of our reconstruction. Prior work at ODP1239 has indicated that sediment source is limited to the Western Cordillera of the northern tropical Andes, particularly from the Guayas, Esmeraldas, and Cayapas rivers in Ecuador (Grimmer et al., 2018, 2020; Rincón-Martínez et al., 2010). Age estimates from this core are based on biostratigraphy and orbital tuning from Timmermann et al. (2007) between 4.956 Ma and 2.7 Ma. For samples younger than 2.7 Ma, we use the age model from Etourneau et al. (2010) that is orbitally tuned. Lastly, we had a single sample at 387.15 meters composite depth below seafloor (mcd) that was outside of either age model available at ODP1239 covering the interval of reconstructed δD_p. For this sample, we assigned the nearest constrained age of 4.956 Ma from Timmermann et al. (2007) at 385.43 mcd. This assigned age is likely ˜20,000 years too young based on the average sedimentation rate at ODP1239 in the interval from 4.956 Ma to 2.7 Ma (Timmermann et al., 2007) but this age uncertainty does not influence any conclusions.

2.3. Leaf Wax Analyses

We reconstructed past changes of water isotopes in precipitation using leaf-wax biomarkers from terrestrial plants that incorporate meteoric waters into their tissues (Sauer et al., 2001; Sternberg, 1988). Leaf waxes are a group of compounds produced by all terrestrial plants to prevent leaf desiccation and environmental damage (Eglinton and Hamilton, 1967). These compounds are likely transported into marine sediments by entrainment in wind or along sediment (Kusch et al., 2010) where they can be preserved in sedimentary archives over geologic timescales (years to millions of years). We analyzed C_{30} *n*-alkanoic acids because they are only produced by terrestrial plants (Kusch et al., 2010; Sachse et al., 2012) and more abundant than C_{29} *n*-alkanes in ODP1239 sediments.

We followed standard analytical methods for extraction, quantification, and compound-specific isotope measurements of *n*-alkanoic acids (Bhattacharya et al., 2018). Sediments were first lyophilized, homogenized, mixed with precombusted diatomaceous earth, and then extracted with a mixture of 9:1 dichloromethane:methanol in a Dionex Accelerated Solvent Extractor 350. A general recovery standard was added to the total lipid extracts to aid in quantification. Fatty acids were purified from the total lipid extracts with column chromatography. We used aminopropyl gel and eluted with 2:1 dichloromethane:isopropanol and 4% acetic acid in DCM for the neutral and acid fractions, respectively. The purified acid fraction was methylated at 50°C overnight using methanol of known isotopic composition to form fatty acid methyl esters (FAME). FAMEs were further purified using 5% deactivated silica gel columns with 100% dichloromethane as an eluent. We quantified FAMEs using a TRACE1310 gas chromatograph equipped with a programmable temperature vaporizer inlet and flame ionization detector. Measurements of δD_{wax} and $\delta^{13}C_{wax}$ were made using a similar TRACE1310 coupled to a Thermo Delta V Plus via a GC-Isolink II device. During analysis, drift was monitored using a synthetic mix of FAMEs every 5 samples (Bhattacharya et al., 2022). Measurements were performed in quadruplicate to achieve a precision greater than 2‰ and 0.2‰ for δD_{wax} and $\delta^{13}C_{wax}$, respectively. We report values after applying mass balance corrections to account for the added methyl group from methylation.

2.4. δD_p reconstructions

A synthesis of C_{29} *n*-alkane plant leaf waxes preserved in surface sediments of lacustrine environments demonstrates a strong linear relationship

between δD_{wax} and δD_p (Sachse et al., 2012). While evapotranspiration can enrich soil and leaf waters in the heavier isotope, wax synthesis in plants preferentially incorporates lighter isotopes of meteoric waters into their tissues, resulting in an apparent fractionation (ϵ_p) and depleted δD_{wax} relative to source water δD_p (Sessions et al., 1999). Plant life form and photosynthetic pathway are primary controls on fractionation. C_3 shrubs and trees and C_4 graminoids represent two fractionation end members: C_3 plants demonstrate a small depletion of water isotopes relative to meteoric waters and C_4 graminoids have a large depletion of water isotopes (Gao et al., 2014; Smith and Freeman, 2006). A similar relationship exists between surveys of plants and δD_p, albeit with more scatter (Sachse et al., 2012). We leveraged this empirical relationship to reconstruct δD_p from measurements of δD_{wax} from ODP1239 in a Bayesian isotope mixing model following Tierney et al. (2017). In this framework, ϵ_p is modeled from measurements of $\delta^{13}C_{wax}$ and contemporary $\delta^{13}C$ from a global survey (Sachse et al., 2012). Once, ϵ_p is determined δD_p is reconstructed using Equation (1) (see Data Availability Statement, Bhattacharya et al., 2018, 2022; Tierney et al., 2017).

$$\delta D_p = \frac{1000 + \delta D_{wax}}{\frac{\epsilon_p}{1000} + 1} - 1000 \tag{1}$$

Concentrations of FAMEs limited the amount of paired δD_{wax} and $\delta^{13}C_{wax}$ measurements. For low concentration samples, we prioritized measuring δD_{wax} and linearly interpolated $\delta^{13}C_{wax}$ to reconstruct δD_p within our Bayesian framework. Reconstructed δD_p is likely insensitive to linearly interpolating $\delta^{13}C_{wax}$ because $\delta^{13}C_{wax}$ never exceeds -27‰(Figure 2), suggesting that C_3 plants dominated the leaf wax source pool. ϵ_p varies little among C_3 plants (Sachse et al., 2012), therefore ϵ_p likely changed minimally at ODP1239.

2.5. Isotope-enabled Community Atmosphere Model simulations

We investigated the influence of equatorial Pacific sea surface temperatures on water isotopes in precipitation in the northern tropical Andes with the isotope-enabled Community Atmospheric Model 5 (iCAM5 Brady et al., 2019; Knapp et al., 2022b). The simulation was initialized using sea surface temperature fields from a Community Earth System Model version 1 simulation that best-captured proxy sea surface temperature reconstructions in the equatorial Pacific (Burls and Fedorov, 2014), particularly the reduced zonal temperature gradient of the early Pliocene (Knapp et al., 2022b). The

applied sea surface temperature field coheres with Mg/Ca sea surface temperature reconstructions that suggest a weakened zonal gradient in sea surface temperatures in the tropical Pacific before 3 Ma (i.e. permanent El-Niño configuration, Fedorov et al., 2006; Wara et al., 2005; White and Ravelo, 2020). However, sea surface temperature reconstructions disagree in the western Pacific and yield conflicting interpretations of the zonal sea surface temperature gradient in the tropical Pacific (Meinicke et al., 2021; Tierney et al., 2019; Wara et al., 2005; White and Ravelo, 2020; Zhang et al., 2014b). Alkenone and TEX_{86} reconstructions indicate higher temperatures than present in the western Pacific and do not support an inferred permanent El Niño-like configuration in the tropical Pacific, though alkenone reconstructions only extend to 4 Ma (Tierney et al., 2019; Zhang et al., 2014b). Despite this disagreement in estimates of western sea surface temperatures in the Pliocene, there is agreement that the eastern equatorial Pacific cold tongue was much warmer than present (Herbert et al., 2016; Lawrence et al., 2006; Tierney et al., 2019; Zhang et al., 2014b). Our iCAM5 simulation includes this warming of the eastern Pacific which enables us to assess the influence that cold tongue warming has on westerly low-level winds into the northern tropical Andes. The simulation was run with $0.9^\circ \times 1.25^\circ$ horizontal resolution and 30 vertical layers for 100 years, of which we average the last 50 years.

The control simulation of iCAM5 captures the seasonal climatology of precipitation, water isotopes in precipitation, and the Choco jet in the northern tropical Andes. Westerly winds associated with the Choco jet increase beginning in May and reach a maximum in September-October-November (SON), after which they decline to a minimum in March-April-May (MAM), as in ERA5 (Figure S3). Alongside the seasonal variability of the Choco jet, iCAM5 captures the northward migration of the Choco jet which is at its most northern extent in SON (Figure S3). Although iCAM5 captures the broad patterns of the contemporary Choco jet well, 925 hPa zonal winds are stronger than estimates from ERA5 (Figure S3). Seasonal variations in δD_p are also captured in the control simulation. GNIP δD_p in Ecuador is largest in December-January-February (DJF), June-July-August (JJA), and SON, with very similar values, and smallest in MAM (Figure 1D). Simulated δD_p is depleted in MAM and enriched in DJF, JJA, and SON, as in GNIP (Figure 1D, S3A). However, δD_p for JJA is too enriched in iCAM5 (Figure 1D, S3A). Precipitation in Ecuador varies with elevation. The lowlands receive 1,500 to 3,000 mm of rainfall annually, with a single wet season from January to April (Garcia et al., 1998; Morán-Tejeda et al., 2016). In the Ecuadorian Andes, to-

tal precipitation decreases to 500 to 1,500 mm of rainfall annually with two wet seasons from March-May and October-November (Garcia et al., 1998; Morán-Tejeda et al., 2016). The $0.9° \times 1.25°$ horizontal resolution of iCAM5 precludes the model from capturing these local elevation effects entirely, but iCAM5 demonstrates some success. Near the Pacific coast simulated precipitation is unimodal with the greatest precipitation from January to May and a pronounced dry season from July to December (Figure S4B). At higher elevations, precipitation reaches a maximum in February, decreases to a minimum in July, and begins to increase steadily after September in iCAM5 (Figure S4B). Despite iCAM5 not accurately simulating bimodal precipitation at high elevations in Ecuador, simulated δD_p compares well with GNIP.

2.6. Eastern equatorial Pacific sea surface temperature synthesis

We compared our leaf wax reconstructions to newly derived indices of Pacific sea surface temperatures. We compiled existing alkenone sea surface temperature records that span the Plio-Pliestocene. The temperature gradient in this region of the eastern equatorial Pacific is closely related to mean sea level pressures and Choco jet variability (Poveda and Mesa, 2000; Sierra et al., 2021). Five alkenone sea surface temperature records in the eastern equatorial Pacific cold tongue span the interval for which we reconstruct δD_p: ODP1239 (Etourneau et al., 2010), ODP850 (Zhang et al., 2014b), ODP846 (Lawrence et al., 2006), IODP U1338 (Rousselle et al., 2013), and ODP847 (Figure 3, Dekens et al., 2007). ODP1241 (Seki et al., 2012) is outside of the influence of the eastern equatorial Pacific cold tongue and represents the off-equatorial region (Figure 3). We calibrated all records using BAYSPLINE (Tierney and Tingley, 2018) and propagated reconstruction errors to the gradient between the cold tongue to off-equatorial regions in the eastern equatorial Pacific with a Monte Carlo resampling approach (Tierney et al., 2019; Bhattacharya et al., 2022).

3. Results and Discussion

3.1. Interpretation of Isotopes

The seasonal climatology of δD_p in Ecuador is controlled by the intensity of westerly water vapor transport and precipitation amount, which is in turn modulated by elevation. GNIP δD_p in Ecuador is depleted in MAM and becomes progressively more enriched throughout the rest of the year (Figure 1D). Similarly, the Choco jet and westerly water vapor transport is weakest in

MAM and increases to a maximum in SON, tracking the position of the ITCZ and convergent tropical easterly winds (Figure 1C, Sierra et al., 2021). When averaged across all GNIP sites in Ecuador, δD_p enriches by ~40‰ following the establishment of the Choco jet in JJA (Figure 1D). This seasonal cycle is enhanced with elevation. GNIP sites at higher elevations along the Western Cordillera exhibit the greatest seasonal change in δD_p. For instance, the lowest elevation GNIP station in Ecuador (6 meters above sea level, masl) has an average δD_p increase of 10‰ when the Choco jet begins to strengthen in JJA (Figure 1D). In contrast, the highest elevation station (3,150 masl) experiences a 60‰ enrichment from MAM to JJA (Figure 1D). The source of enriched water vapor is likely the Eastern Pacific Warm Pool, which may be amplified by processes like Rayleigh distillation and water vapor recycling (Salati et al., 1979) during transport into Ecuador. Water vapor isotopic composition measured from the Tropospheric Emission Spectrometer aboard the Aura Earth satellite demonstrates that δD_{vapor} is highly enriched in the Eastern Pacific Warm Pool (Figure S5). Westerly winds are strong over this region of enriched water vapor and extend into Ecuador (Figure 1A, S5). In MAM, this region of enriched δD_{vapor} extends into Ecuador aligning with depleted δD_p at the GNIP stations (Figure S5). This spatial overlap explains the linear relationship between the Choco jet index and δD_p (Figure 1A). A stronger Choco jet transports enriched water vapor from the Eastern Pacific Warm Pool and increases δD_p in Ecuador. Lagrangian trajectory analyses for the Pacific coast of Colombia also indicate the importance of Pacific water vapor sources in months when westerly winds are strongest (Hoyos et al., 2018; Sakamoto et al., 2011).

The precipitation amount effect that is commonly observed in tropical records of water isotopes in precipitation has a limited influence on δD_p in Ecuador. The precipitation amount effect is defined as the inverse relationship between the isotopic signature of precipitation and precipitation amount (Dansgaard, 1964). This relationship is thought to emerge, in part, because cooling rain clouds remove heavier isotopologues and rain drop re-evaporation decreases as humidity increases during precipitation (Dansgaard, 1964; Rozanski et al., 1993). From our linear mixed-effects models, we find that the Choco jet index is a stronger predictor of δD_p than monthly precipitation amount. When the Choco jet index is the only predictor, linear mixed-effects model fit is better than when precipitation amount is the only predictor (13.12 higher log-likelihood and 26.24 lower AIC, Table S1). This pattern holds when adding the Choco jet index and precipitation amount as

secondary predictors. Monthly precipitation amount as an additional predictor to the Choco jet index only marginally improves linear mixed effect model fit (2.32 increase in log-likelihood, 2.65 decrease in AIC, Table S1). In contrast, the Choco jet index as an additional predictor to monthly precipitation amount greatly improves linear mixed effect model fit (15.44 increase in log-likelihood, 28.89 decrease in AIC, Table S1). Findings from the linear mixed-effects models are congruent with the nonlinear relationship between monthly precipitation amount and δD_p in Ecuador (Figure 1B). The relationship between the Choco jet index and δD_p is comparatively linear, especially when considering elevation (Figure 1A). However, at individual GNIP sites, the amount effect does emerge. For example, the Espoch (2,820 masl), Quito-Inamhi (2,789 masl), and Cuenca (2,510 masl) GNIP stations appear to have a linear relationship between precipitation amount and δD_p (Garcia et al., 1998). Integrating over a large area, as we do here, causes water vapor sources to overprint local amount effects. For these reasons, we find that δD_p on the Western Cordillera of Ecuador is primarily controlled by changes in westerly water vapor transport from the Eastern Pacific Warm Pool and that reconstructed δD_p at ODP1239 records variations in this transport through the Plio-Pleistocene.

3.2. δD_p trends at ODP1239

Reconstructed δD_p at ODP1239 exhibits a gradual enrichment with a depletion at ~3 Ma (Figure 2B). Reconstructed δD_p values in the earliest portion of the record (5.0 to 4.6 Ma) are among the most depleted, averaging -9.5‰ and suggest weak westerly transport from the Eastern Pacific Warm Pool during the early Pliocene. After the early-Pliocene, δD_p enriched by 5.6‰ into the mid-Piacenzian warm period (3.264 - 3.025 Ma) (Figure 3A) which indicates a strengthening of westerly transport of enriched water vapor from the Eastern Pacific Warm Pool. A rapid depletion of 14.3‰ from 3 to 2.7 Ma is synchronous with large-scale changes in the Earth system (Figure 3C), after which δD_p increases by 5.9‰ and marks the end of the Pliocene. This rapid depletion is coincident with the onset of major Northern Hemisphere glaciation (Raymo, 1994), though the exact timing of glaciation events remains debated. The Pleistocene section of ODP1239 mirrors the Pliocene with an overall trend of enrichment that is interrupted by an abrupt increase in δD_p of 10.0‰ from 1.7 to 1.6 Ma, synchronous with increases in sea surface temperatures of 1.65 and 0.42 °C in the eastern Pacific Cold tongue, as reconstructed from the alkenone paleothermometer at ODP1239

and ODP846, respectively (Figure S6, Etourneau et al., 2010; Lawrence et al., 2006; Seki et al., 2012). The relationship between variations in westerly water vapor transport and global to regional climate changes suggests potential controls on the dynamics that govern the position and strength of westerly transport.

A gradual enrichment of δD_p at ODP1239 suggests that changes in Andean topography had little impact on reconstructed δD_p through the Plio-Pleistocene. Evidence from thermochronological constraints (Spikings et al., 2001, 2010; Villagómez and Spikings, 2013), detrital zircon typology coupled with U/Pb geochronology (Osorio-Granada et al., 2017), provenance analyses (León et al., 2018), fossil pollen (Grimmer et al., 2018), and zircon geochronology (Echeverri et al., 2015) collectively suggest the presence of significant topography in the Western Cordillera by the late-Miocene/early-Pliocene. However, exhumation rates increase after 15 Ma from the subduction of the Carnegie Ridge and suggest surface uplift (Margirier et al., 2023; Spikings et al., 2001; Spikings and Simpson, 2014). Any surface uplift after 5 Ma would have imposed a trend of depletion because water isotopes in precipitation become depleted as elevation increases (Figure 1, Ambach et al., 1968). Nevertheless, δD_p at ODP1239 exhibits gradual enrichment, indicating no influence from elevation changes. This conflicting interpretation suggests that Andean uplift did not significantly affect δDp at ODP1239.

3.3. Westerly moisture transport variability and hydroclimate changes during the Pliocene

Variations in westerly water vapor transport during the Plio-Pleistocene are associated with changed hydroclimate and ecological turnover in the northern tropical Andes through a coupling with the South Pacific Subtropical High. When the Choco jet is strong, precipitation increases in Colombia and decreases in Peru/Chile (Figure 3E). This likely occurs because the Choco jet, in part, forms from winds on the eastern edge of the South Pacific Subtropical High (Sierra et al., 2021). In the seasonal cycle the Choco jet and westerly water vapor transport and the South Pacific Subtropical High are all strongest in SON (Figure S3A, Fahad et al., 2021). A strong South Pacific Subtropical High transports more moisture northward from the southern Pacific and associated subsidence dries Chile (Barrett and Hameed, 2017; Quintana and Aceituno, 2012). In MAM, the Choco jet and South Pacific Subtropical High are weak (Figure S3A, Fahad et al., 2021). A weakened South Pacific Subtropical High reduces subsidence over Chile/Peru and

increases precipitation (Barrett and Hameed, 2017; Quintana and Aceituno, 2012). Based on this relationship, weakened westerly water vapor transport during the early Pliocene (Figure 3C) suggests precipitation decreased in western Colombia and increased in western Peru/Chile (Figure 3E) from a weakening of the South Pacific Subtropical High. iCAM5 simulations for the early Pliocene are consistent with these expectations. Positive precipitation anomalies in Chile and Peru are matched with negative precipitation anomalies in western Colombia and a decrease in the strength of the South Pacific Subtropical High (Figure 4B). High stream erosion and incision in the Atacama Desert support high inferred precipitation in the early Pliocene in Chile (Amundson et al., 2012; Hartley and Chong, 2002). This geomorphic evidence also points to brief periods of 'extreme' precipitation following the mid-Pliocene drying of the Atacama Desert (Amundson et al., 2012). A depletion of δD_p at ODP1239 at the start of the Pleistocene (Figure 3C, E) suggests a brief interval of weakening in the South Pacific Subtropical High that could produce the conditions necessary for 'extreme' precipitation in the Atacama Desert.

Ecological turnover inferred from fossil pollen in the early Pliocene at ODP1239 highlights the role that long-term changes in regional atmospheric circulation can have on ecosystem structure. Reduced westerly water vapor transport into Ecuador during the early Pliocene (Figure 3A) is associated with a high abundance of taxa such as Cyperaceae and Ilex that generally prefer wetter climates (Figure 3D, Grimmer et al., 2018; Marchant et al., 2002). As westerly water vapor transport increased during the mid-Pliocene these taxa declined in abundance (Figure 3A, D). An indicator of lowland drying, Amaranthaceae prefers drier coastal environments and is in low abundance until the mid-Pliocene (Figure 3D, Grimmer et al., 2020). The shared decline in taxa that prefer humid conditions, an increase in Amaranthaceae, and an increase in westerly water vapor transport are consistent with interannual variations in precipitation in Ecuador. In the present-day, El Niño events increase precipitation in coastal Ecuador (Morán-Tejeda et al., 2016) and weaken westerly water vapor transport (Poveda et al., 2006). Hence, weakened westerly water vapor transport in the early Pliocene may be linked to increased precipitation in Ecuadorian lowlands, supporting taxa that prefer humid conditions (Figure 3A, E Grimmer et al., 2018). Accordingly, a strengthening of westerly water vapor transport in the mid-Pliocene would be paired with precipitation decrease in the Ecuadorian lowlands, enabling Amaranthaceae to expand (Figure 3A, E, Grimmer et al., 2020). Fossil pollen from

ODP1239 is assumed to be mostly fluvially sourced (Grimmer et al., 2018, 2020), but eolian deposits are likely also an important contributor (Heusser and Shackleton, 1994). Winds along the Pacific coast of South America are predominantly from Chile (Strub et al., 1998) where conditions were wetter during the early Pliocene (Amundson et al., 2012; Hartley and Chong, 2002) and may have contributed to the high abundance of taxa that prefer humid conditions at ODP1239. Hypothesized precipitation changes in Ecuador require further testing because the relationship between the Choco jet and annual precipitation is weak (Figure 3E). Moreover, pollen may be responding to localized coastal convection in Ecuador, while isotopes reflect large-scale changes in vapor transport. Long distance pollen dispersal may further confound pollen-based climate interpretations. More records are needed to establish spatial patterns of precipitation changes in the northern tropical Andes during the Pliocene.

3.4. Evolving controls on the Choco jet through the Plio-Pleistocene

Atmospheric circulation in the northern tropical Andes responded to evolving controls through the Plio-Pleistocene, with two regimes separated by the initiation of Northern Hemisphere cooling. Sea surface temperatures in the eastern equatorial Pacific emerge as an important control on the westerly transport of enriched water vapor into the northern tropical Andes through the Pliocene. At present, the cold tongue to off-equatorial pressure and temperature gradients in the eastern Pacific drive interannual variability in the Choco jet (Sierra et al., 2021). Across the Pliocene, sea surface temperatures between the cold tongue and off-equatorial regions evolved asymmetrically (Figure 3B, S6D-H, Tierney and Russell, 2007). The difference in sea surface temperatures between the eastern equatorial Pacific cold tongue and ODP1241 (5°50.57′ N, 86°26.68′W), in the Eastern Pacific Warm Pool, is at a minimum during the early Pliocene and increases to present (Figure 3B). This configuration of sea surface temperatures would produce a low mean sea level pressure gradient (Lindzen and Nigam, 1987) and weak westerly winds, consistent with depleted δD_p. A similar process occurs during modern El Niño events that force the Choco jet to weaken as the cold tongue warms and the mean sea level pressure gradient decreases from the cold tongue to the off-equatorial eastern Pacific (Poveda et al., 2006). The eastern equatorial Pacific cold tongue upwells water from depth, and after ˜3 Ma a regional shoaling of the thermocline cooled the cold tongue more than regions to the north near the Warm Pool(Ford et al., 2015) (Figure 3). Accordingly, as

the sea surface temperature gradient from the eastern equatorial Pacific cold tongue to ODP1241 increases in the mid- to late-Pliocene, so too does δD_p. A larger sea surface temperature gradient would have increased westerly transport of enriched δD_{vapor} from the Eastern Pacific Warm Pool increasing δD_p at ODP1239 (Figure 3A,B, S6D-H).

A decline in westerly water vapor transport at ˜3 Ma points to an increasing influence of high latitude forcings. The inception of major Northern Hemisphere glaciation (Raymo, 1994) would have altered global energy budgets as the Northern Hemisphere cooled more than the Southern Hemisphere from expansive ice sheets (Chiang and Bitz, 2005). Interhemispheric energetic imbalances imposed by the addition of ice in the Northern Hemisphere shift the ITCZ southward towards the equator in climate simulations, from its mean position in the Northern Hemisphere (Chiang et al., 2003; Chiang and Bitz, 2005; Schneider et al., 2014). The westerly winds that flow into the northern tropical Andes develop from southerly winds which follow the low mean sea level pressure of the ITCZ and are deflected eastward by Coriolis acceleration which changes direction across the equator (Sierra et al., 2021). Shifting the ITCZ southward from the inception of major Northern Hemisphere glaciation would reduce Coriolis acceleration acting on southerly cross equatorial winds, in turn reducing the westerly flow that fuels the jet. An inferred ITCZ shift is supported by salinity data: sea surface salinity reconstructions from $\delta^{18}O_{salinity}$ at ODP1241 demonstrate a decline of 0.77 ‰ at 2.95 Ma, consistent with a southward shift in the ITCZ. This salinity drop is synchronous with reduced westerly water vapor transport, after which freshening accelerates (Figure 3A,C). $\delta^{18}O_{salinity}$ at ODP1241 begins to indicate freshening at 3.7 Ma suggesting the connection between Northern Hemisphere cooling, ITCZ position, and westerly wind strength in the eastern equatorial Pacific is complex. The apparent decoupling between the ITCZ, westerly winds, and salinity at ODP1241 before 3.7 Ma may, partly, be the result of the exchange of water vapor between the eastern equatorial Pacific and the Caribbean. Topography was low during the formation of the Isthmus of Panama, with periods of water mass exchange as recent as 2.58 Ma (Groeneveld et al., 2014), and was likely lower still during the early Pliocene. The Isthmus of Panama has undergone continuous uplift since ˜6 Ma (O'Dea et al., 2016) indicating that topographic barriers to water vapor transport from the Atlantic Ocean to the Pacific Ocean was low in the early Pliocene, possibly obscuring the relationship between ITCZ position and precipitation isotopes early in the ODP1239 record. Grain size analyses

from ODP848 and ODP849, support an inferred shift of the ITCZ at 3 Ma from $\delta^{18}O_{salinity}$. Mean grain size increases briefly around 3 Ma suggesting stronger easterlies near the equator consistent with idealized climate model experiments that place a large ice sheet in the Northern Hemisphere (Broccoli et al., 2006).

3.5. Paired δD_p, Choco jet, and westerly water vapor transport changes in iCAM5

Our early Pliocene-like iCAM5 simulations support our hypothesized link between changes in the cold tongue to off-equatorial sea surface temperature gradient in the eastern Pacific and westerly wind strength. The model is forced with a small tropical Pacific sea surface temperature gradient (meridional and zonal) that forces a decrease in δD_p, which coheres with the direction of the signal at ODP1239. The magnitude of δD_p depletion in iCAM5 is smaller than reconstructed δD_p at ODP1239 for the early Pliocene and consistent with prior proxy-model comparisons (Figure 2B, 4). Generally, isotope-enabled climate models reproduce a smaller isotopic change than shown by proxies (Hu et al., 2018). Depleted δD_p in iCAM5 is likely driven by circulation changes, since the model simulates weakened westerly water vapor transport in the core Choco jet region (Figure 4A). A reduction in westerly wind strength is greatest in JJA and SON (Figure S7) when the Choco jet and westerly water vapor transport is at its climatological maximum (Figure S3). Furthermore, simulated precipitation changes are not spatially coherent with δD_p in the northern tropical Andes, suggesting that δD_p fluctuations are not caused by precipitation amount in iCAM5 (Figure 4C, D). We hypothesize that upstream changes in δD_p in iCAM5 helps deplete δD_p in Ecuador. iCAM5 has an inverse linear relationship between stratiform rainfall amount and preciptiation isotopes (Hu et al., 2018). The proportion of stratiform rainfall increases in the central tropical Pacific which depletes δD_p. Integrated water vaport transport anomalies show greater transport from the central tropical Pacific where δD_p decreases and stratiform rainfall fraction increases are greatest (Figure 5).

Reduced regional and basin-wide sea surface temperature gradients in the tropical Pacific force a weakening of the Choco jet and westerly winds into the northern tropical Andes in iCAM5. Sea surface temperature reconstructions disagree in the western Pacific and yield conflicting interpretations of the zonal sea surface temperature gradient in the tropical Pacific. Forced sea surface temperature fields in our iCAM5 simulation are mostly unchanged

from the control simulation in the western Pacific, but are much higher in the eastern Pacific, resembling a permanent El Niño-like climate state (Knapp et al., 2022b). A reduced zonal sea surface temperature gradient in the tropical Pacific may also explain a weaker Choco jet (Figure 4) on top of the influence of the cold tongue/off-equatorial gradient of temperature in the eastern equatorial Pacific. A low zonal sea surface temperature gradient in the tropical Pacific weakens the Walker Circulation and lowers mean sea level pressure over the eastern Pacific (Bjerknes, 1969). Westerly winds into the northern tropical Andes are partly driven by high mean sea level pressure over the eastern equatorial cold tongue (Poveda and Mesa, 2000; Poveda et al., 2014; Sierra et al., 2018). These winds would weaken as mean sea level pressures fall in the eastern Pacific. Hence, a low zonal sea surface temperature gradient in the tropical Pacific and a permanent El Niño-like state is consistent with weakened westerly transport inferred at ODP1239 in the early Pliocene (Figure 3A).

Our results suggest that the northern tropical Andes is strongly sensitive to alternative configurations of tropical Pacific temperature gradients in isotope-enabled climate models. Basin-wide zonal and meridional sea surface temperature gradients in the Pacific contribute to establishing global atmospheric circulation and climate patterns. Reconstructing these spatial gradients through the Plio-Pleistocene has received considerable attention using estimates of sea surface temperature (Fedorov et al., 2015; Tierney et al., 2019; Wara et al., 2005; Zhang et al., 2014a) but proxies sensitive to atmospheric circulation are underutilized. In the northern tropical Andes, modern and past variations in westerly winds respond to regional (e.g. cold tongue to off-equatorial) and basin-wide (e.g. western to eastern Pacific) sea surface temperature gradients in the tropical Pacific (Poveda and Mesa, 2000; Sierra et al., 2021). In turn, westerly water vapor transport controls δD_p in the northern tropical Andes. Our findings suggest that records of δD_p in the northern tropical Andes are an important benchmark for constraining the evolution of sea surface temperature and atmospheric circulation across the tropical Pacific.

4. Conclusions

Westerly winds are a key feature of atmospheric circulation in the northern tropical Andes, particularly those concentrated in the Choco jet (Poveda and Mesa, 2000). Climate models (Sierra et al., 2021) and proxy reconstruc-

tions (Martínez et al., 2003) demonstrate the sensitivity of the Choco jet to changes in the mean climate, but proxy evidence for greenhouse climate states has been sparse. We develop a new record of δD_p from ODP1239 reconstructed from C_{30} *n*-alkanoic acids that span the Pliocene and Pleistocene to address this uncertainty. Our analysis of observational δD_p from GNIP stations in Ecuador demonstrates westerly winds in the eastern equatorial Pacific transport enriched water vapor from the Eastern Pacific Warm Pool (Figure 1, S5). When westerly winds are weakest, δD_p is depleted in Ecuador, becoming enriched as westerly winds strengthen in JJA transporting enriched water vapor. Applying this contemporary relationship to reconstructed δD_p from ODP1239 suggests that westerly winds were weak during the early Pliocene and gradually strengthened to the present. A key driver of these winds is the cold tongue to off-equatorial sea surface temperature gradient in the eastern Pacific, and this gradient was at a minimum in the early Pliocene. In an early Pliocene iCAM5 simulation, δD_p decreases in the northern tropical Andes from a weakening of westerly water vapor transport and increased transport of depleted water vapor from upstream sources. The trend of gradual enrichment of δD_p through the Pliocene suggests little to no influence of Andean uplift on δD_p. Gradual enrichment is interrupted by depletion at ~3 Ma, coincident with the onset of major Northern Hemisphere cooling (Raymo, 1994). We hypothesize that this depletion is caused by extratropically-forced shifts in the configuration of the Southern Hemisphere Hadley Cell and the ITCZ. A similar mechanism could have operated on glacial/interglacial timescales but requires higher resolution records to test this hypothesis. The weakening of westerly water vapor transport in response to decreases in regional sea surface temperature and mean sea level pressure gradients that emerge in our proxy-model comparison agrees with projected changes to the Choco jet by the end of the 21st century. Under high emission scenarios, projections demonstrate a weakening and southward shift of the Choco jet as the mean sea level pressure gradient between the eastern Pacific cold tongue and the northern tropical Andes decreases (Sierra et al., 2021), with implications for regional ecosystems, biodiversity, and hydroclimate-related risks.

4.1. Acknowledgements

TB and RF acknowledge funding from NSF P2C2 award OCE-2103015. NJB and SK acknowledge funding support from NSF Award AGS-1844380. LPA acknowledges funding support from NSF SGP award 1929199. We thank

the Integrated Ocean Drilling Program, especially the Gulf Coast Repository, for providing the sediment for site 1239. Discussions with Claire Rubbelke, Peter Brennan, Helbert Schneider Garcia Delgado, and Stephanie Bullinger greatly improved the manuscript and visualizations. The PaleoX seminar series provided great feedback and support throughout the development of this manuscript.

4.2. Data Availability Statement

All data and code used in this study are available on Zenodo (Fastovich et al., 2023). The new δD_p record for ODP1239 is also available on the NOAA NCEI Paleoclimatology database. iCAM5 results are available on Zenodo (Knapp et al., 2022a).

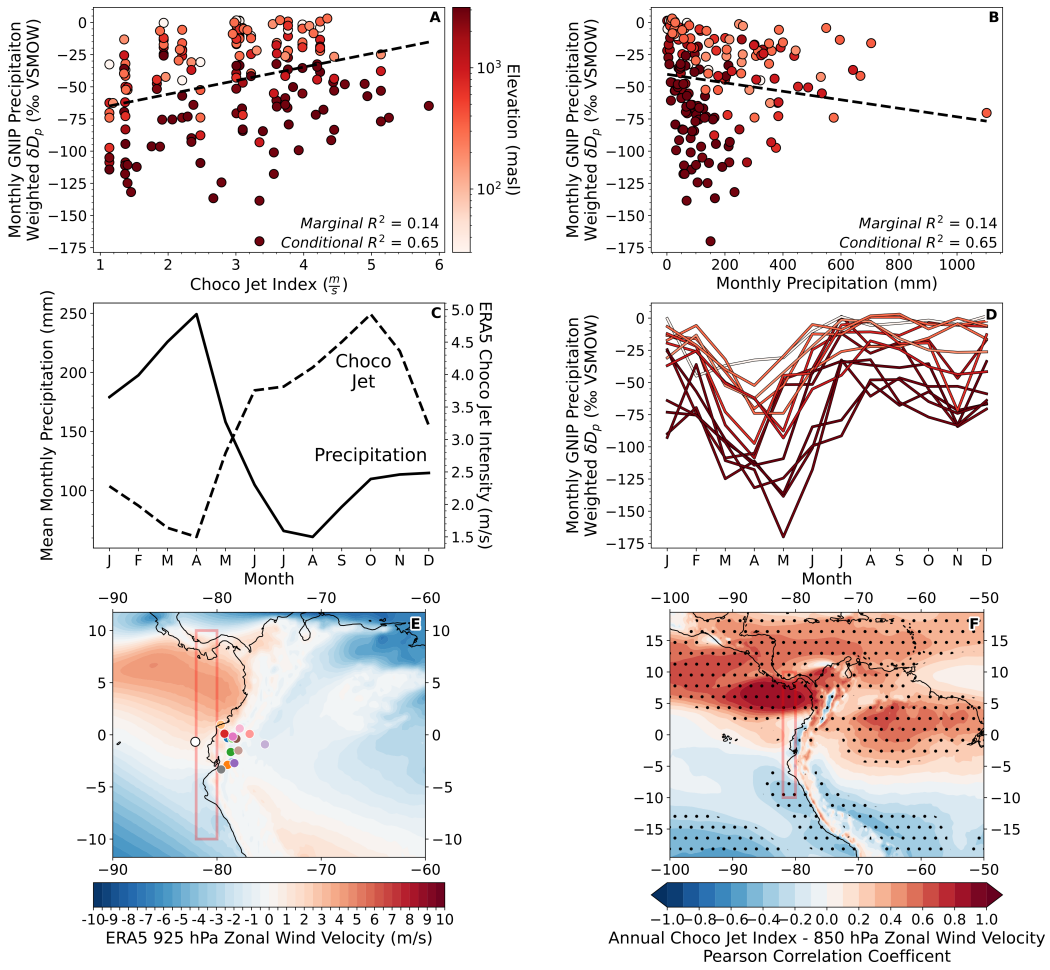

Figure 1: The linear relationship between monthly averaged δD_p from GNIP stations and (A) the Choco jet and (B) monthly precipitation. The dashed line represents the mean fit of a linear mixed-effect model with Choco jet index and monthly precipitation amount as predictors and elevation as a random variable (model 2 in Table S1). Colors correspond to GNIP station elevation. (C) Monthly averaged precipitation from GNIP stations in Ecuador and Choco jet intensity. (D) The monthly climatology of δD_p from all GNIP stations colored by elevation, as in (A) and (B). (E) The SON climatology of 925 hPa zonal winds from ERA5 between the period 1959 and 2022 with GNIP stations marked as points. ODP1239 is located off the coast of Ecuador and is labeled by a white point. (F) The correlation between the Choco jet index (Sierra et al., 2021) and 850 hPa zonal winds from ERA5. The red box denotes the region used when calculating the Choco jet index as defined in Sierra et al. (2021). Note, all δD_p averages are precipitation weighted. The legend for (E) is located in Figure S1.

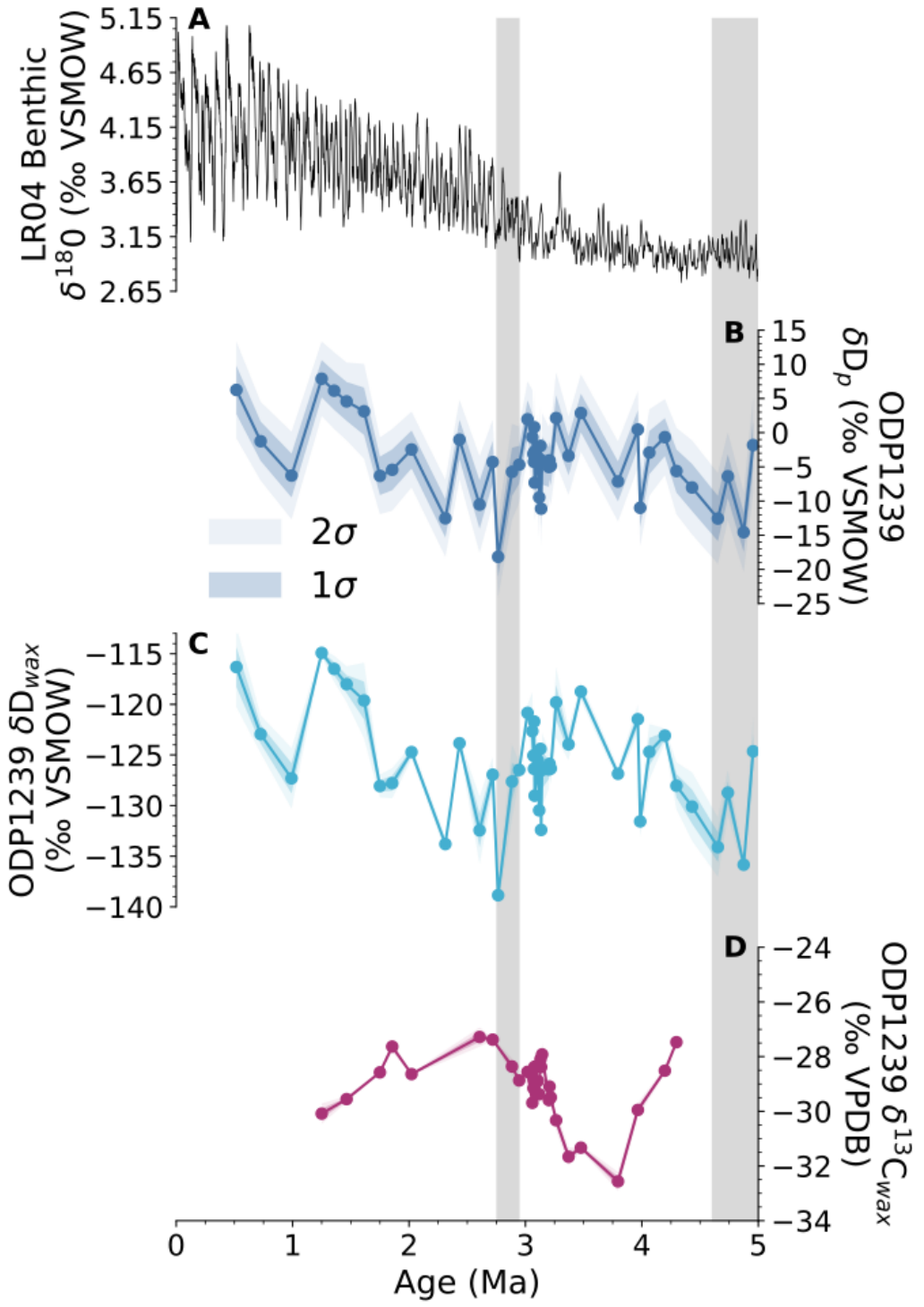

Figure 2: (A) Globally averaged benthic foraminifer δ^{18}O (Lisiecki and Raymo, 2005). (B) Reconstructed δD_p at ODP1239. (C, D) Measured δD_{wax} and $\delta^{13}C_{wax}$ from C_{30} n-alkanoic acids at ODP1239. The shaded area corresponds to the early Pliocene (5.0 to 4.6 Ma) and the onset of major Northern Hemisphere glaciation (3.0 to 2.75 Ma).

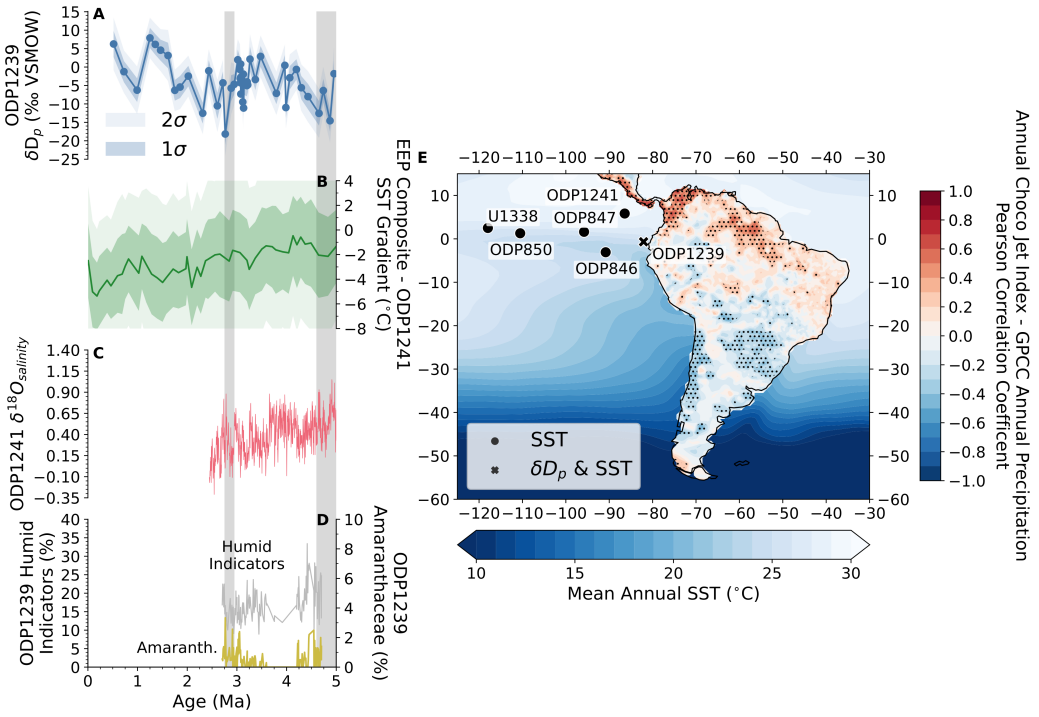

Figure 3: (A) Reconstructed δD_p at ODP1239. (B) The sea surface temperature gradient between the eastern equatorial Pacific cold tongue composite and ODP1241 which has a close correspondence to Choco jet strength (Sierra et al., 2021). (C) Reconstructed sea surface salinity based on $\delta^{18}O$ from ODP1231 that serves as a record of ITCZ position (Groeneveld, 2005). (D) Fossil pollen-based indicators of humidity and aridity (Amaranthaceae) at ODP1239 as percent abundance (Grimmer et al., 2018, 2020). The shaded area corresponds to the early Pliocene (5.0 to 4.6 Ma) and the onset of major Northern Hemisphere glaciation (3.0 to 2.75 Ma). (E) For South America, the color corresponds to the Pearson correlation coefficient between the Choco jet index and annual precipitation from the Global Precipitation Climatology Centre (GPCC) (Schneider et al., 2011) between the period 1959 and 2022. Stippling indicates significance at the 95% confidence level based on a Student's t-test. For oceans, the shading corresponds to the mean annual sea surface temperature averaged between 1891 and 2023 from the COBE-SST data product (Ishii et al., 2005).

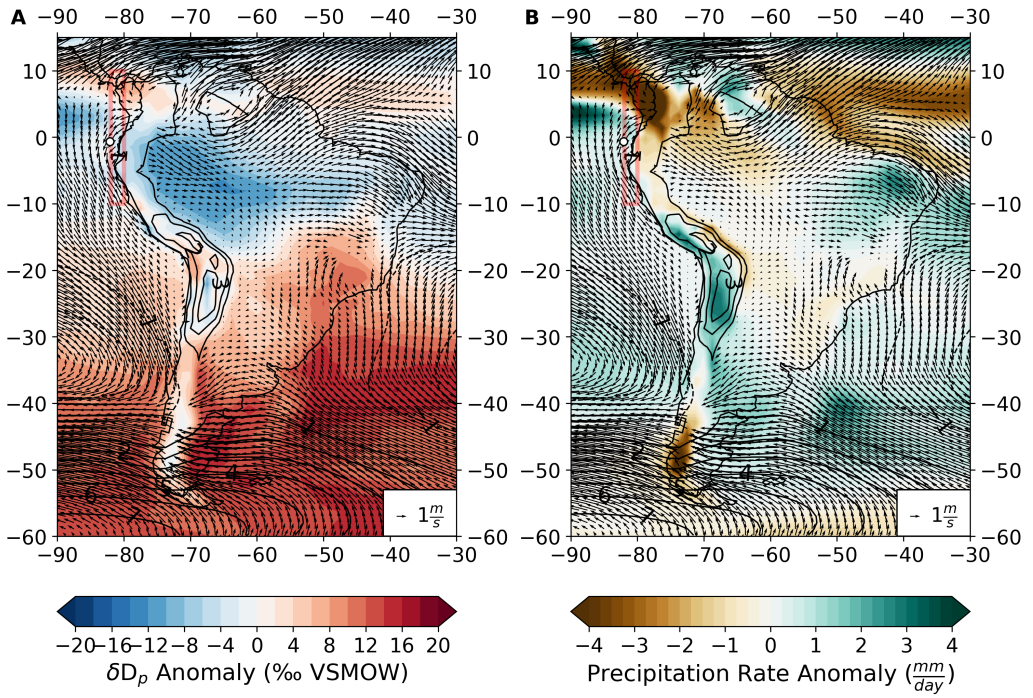

Figure 4: Annual climatological anomalies (early Pliocene experiment - control) from iCAM5 (Knapp et al., 2022b) for (A) δD_p and (B) precipitation rate forced with a reduced tropical Pacific zonal sea surface temperature gradient. Contours represent mean annual sea level pressure anomalies with the zero contour omitted. Vectors correspond to wind anomalies at 925 hPa, where the Choco jet core is found (Poveda and Mesa, 2000; Sierra et al., 2021). ODP1239 is located off the coast of Ecuador and is labeled by a white point. The red box corresponds to the region used to calculate the Choco jet index.

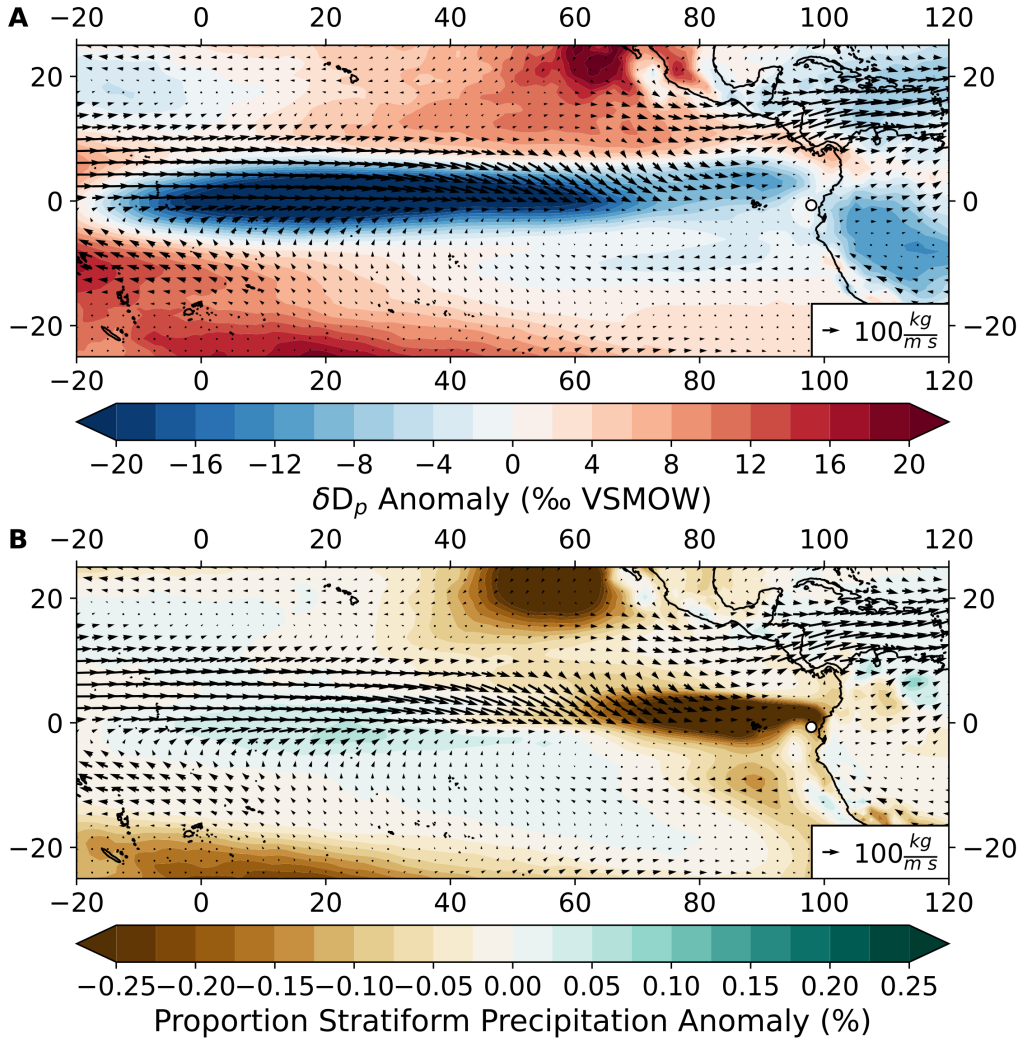

Figure 5: Simulated (A) δD_p and (B) proportion stratiform rainfall anomalies from iCAM5 (early Pliocene experiment - control, Knapp et al., 2022b). Vectors in (A) and (B) correspond to integrated water vapor transport anomalies from the surface to 200 hPa calculated using $\frac{1}{g}\int_{surf}^{200} q\mathbf{V}\,dp$, where g is gravitational acceleration, q is specific humidity, and the vector $\mathbf{V}$ represents the meridional and zonal components of wind.

5. Supplemental Tables and Figures

	Model	Conditional R^2	Marginal R^2	Log-Likelihood	AIC
1	Monthly Weighted $\delta D_p \sim 1 +$ random(Elevation)	0.42	0	-869.08	1744.16
2	Monthly Weighted $\delta D_p \sim$ Choco Jet Index + Monthly Precipitation + random(Elevation)	0.65	0.14	-841.94	1693.87
3	Monthly Weighted $\delta D_p \sim$ Choco Jet Index + random(Elevation)	0.62	0.13	-844.26	1696.52
4	Monthly Weighted $\delta D_p \sim$ Monthly Precipitation + random(Elevation)	0.59	0.10	-857.38	1722.76
5	$\sqrt[3]{\text{Monthly Weighted } \delta D_p} \sim 1 +$ random(Elevation)	0.40	0	-277.07	560.15
6	$\sqrt[3]{\text{Monthly Weighted } \delta D_p} \sim$ Choco Jet Index + Monthly Precipitation + random(Elevation)	0.63	0.16	-251.55	513.10
7	$\sqrt[3]{\text{Monthly Weighted } \delta D_p} \sim$ Choco Jet Index + random(Elevation)	0.56	0.11	-257.93	523.86
8	$\sqrt[3]{\text{Monthly Weighted } \delta D_p} \sim$ Monthly Precipitation + random(Elevation)	0.60	0.14	-260.42	528.84

Table S1: The linear mixed-effects models tested to determine the climatological controls on Monthly Weighted δD_p from GNIP and the resulting conditional R^2, marginal R^2, log-likelihood, and Akaike information criterion as model diagnostics (Akaike, 1973; Nakagawa and Schielzeth, 2013). The random(Elevation) term corresponds to the random effect of station elevation, thereby allowing different intercepts for the fixed effect in the linear mixed-effects model (i.e. the same slope but with different intercepts). This term was included in all models tested because the relationship between Monthly Weighted δD_p varies strongly by elevation.

Figure S1: The list of GNIP stations used for analyses in Figure 1 and the legend for Figure 1E, F.

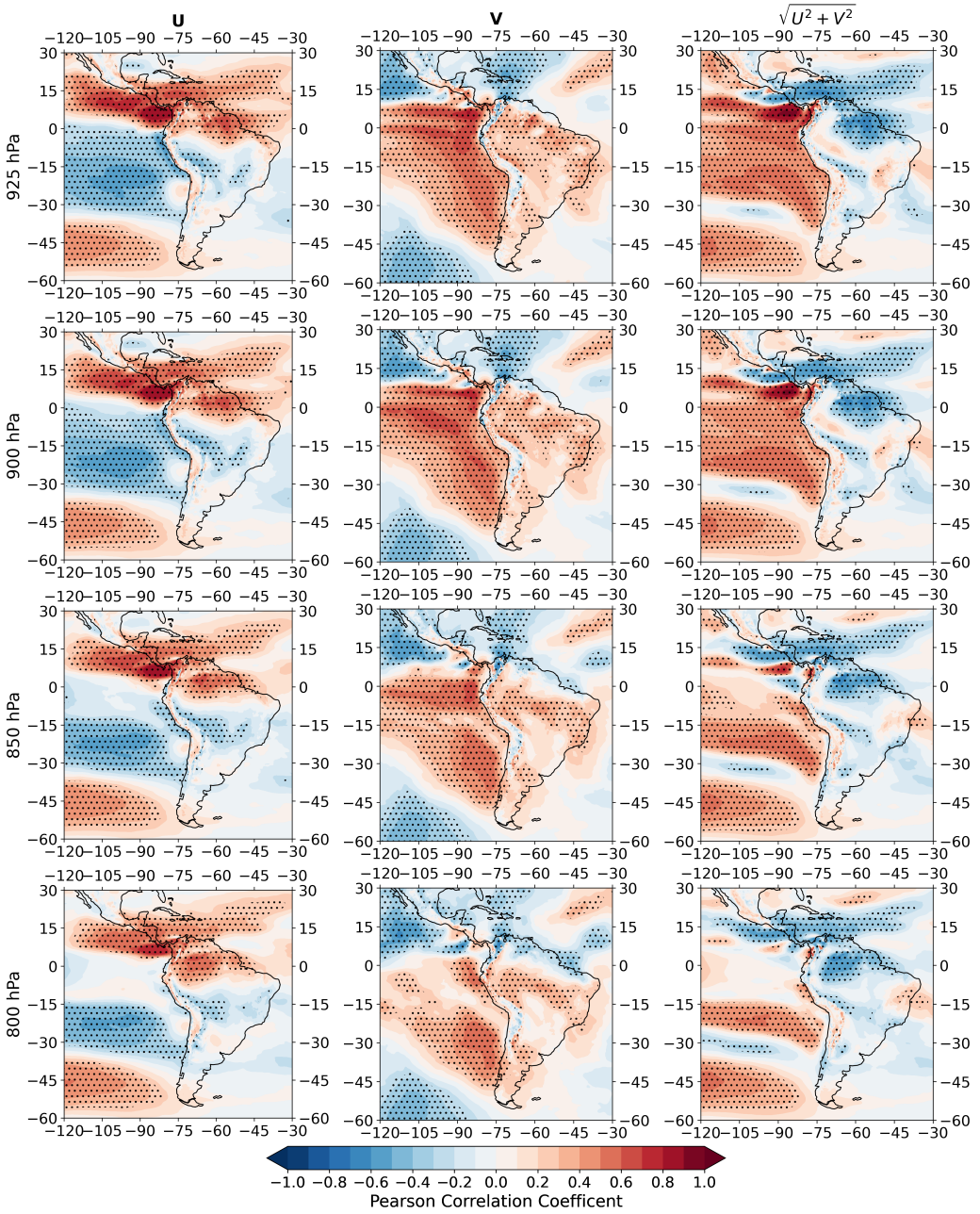

Figure S2: The correlation between the Choco jet index proposed in Sierra et al. (2021) and zonal, meridional, and wind magnitude at the 925, 900, 850, and 800 hPa pressure levels calculated based on data from ERA5 for annual averages between 1959 and 2022 (Hersbach et al., 2020). Each column corresponds to a correlation between the Choco jet index and a different component of wind. Each row corresponds to a different pressure level. Stippling indicates significance at the 95% confidence level based on a Student's t-test. At all pressure levels, the Choco jet is correlated with westerly transport from the eastern equatorial Pacific, where δD_p is enriched (Figure S5), into Ecuador.

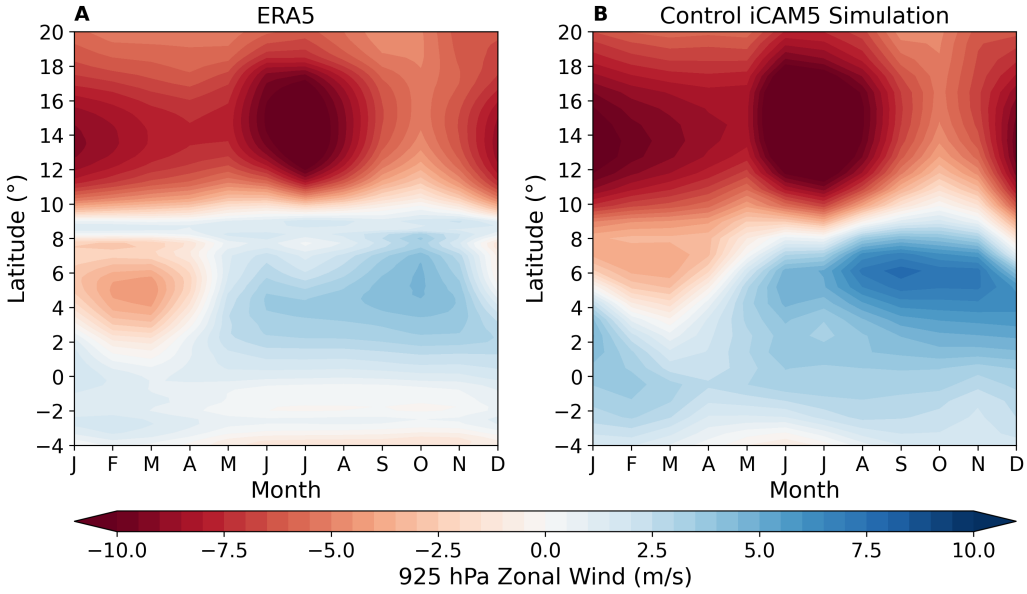

Figure S3: Hövmoller diagrams of 925 hPa zonal winds at 81 °W from (A) ERA5 (Hersbach et al., 2020) and (B) the control iCAM5 simulation (Knapp et al., 2022b). The control iCAM5 simulation captures the meridional migration of the Choco jet and strengthening in SON. The climatology for ERA5 is based on the period 1959 to 2022.

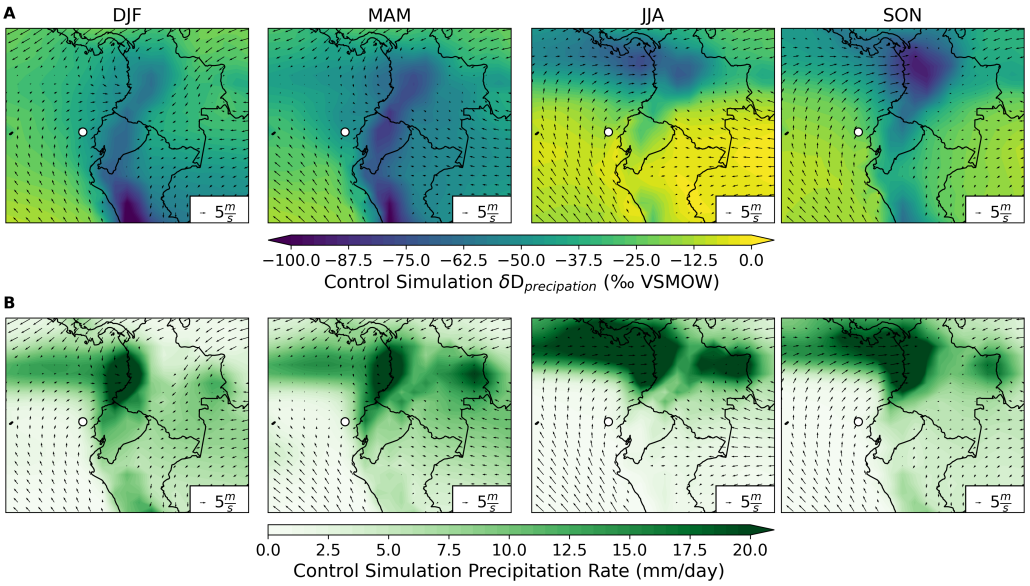

Figure S4: Seasonal climatology of (A) δD_p and (B) precipitation from the control iCAM5 simulation (Knapp et al., 2022b). Depleted δD_p from GNIP stations in Ecuador are captured, as is the unimodal precipitation regime (Figure 1). The location of ODP1239 is labeled as a white point.

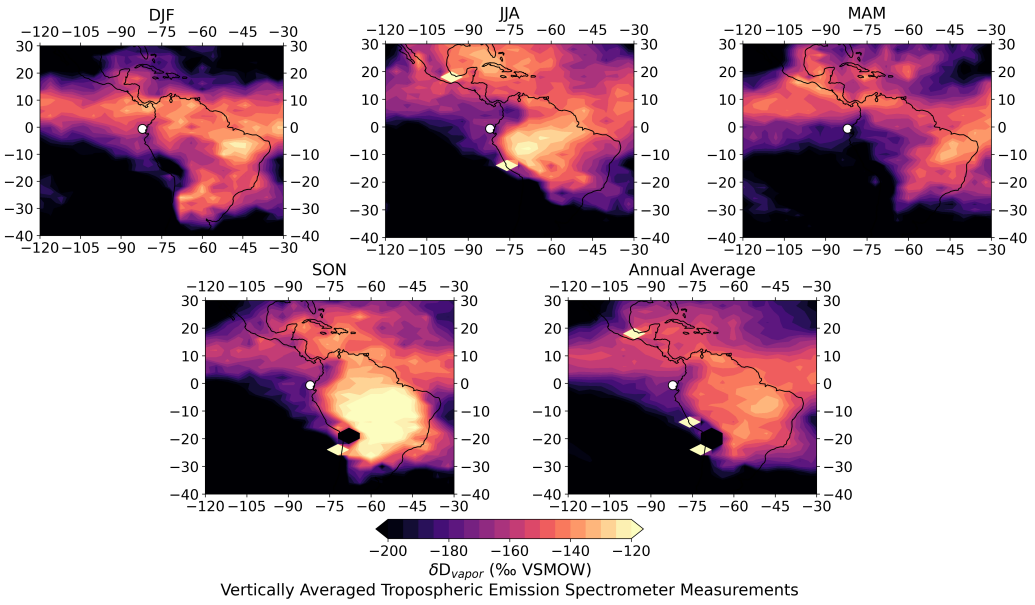

Figure S5: The seasonal and annual climatology of pressure-weighted δD_{vapor} averaged between 825 and 450 hPa based on the Version 4 Level 3 Tropospheric Emission Spectrometer satellite data product for the years 2006, 2007, 2008, and 2009. Note the enriched δD_{vapor} from the eastern Pacific ITCZ extending to the northern tropical Andes for all seasons except MAM.

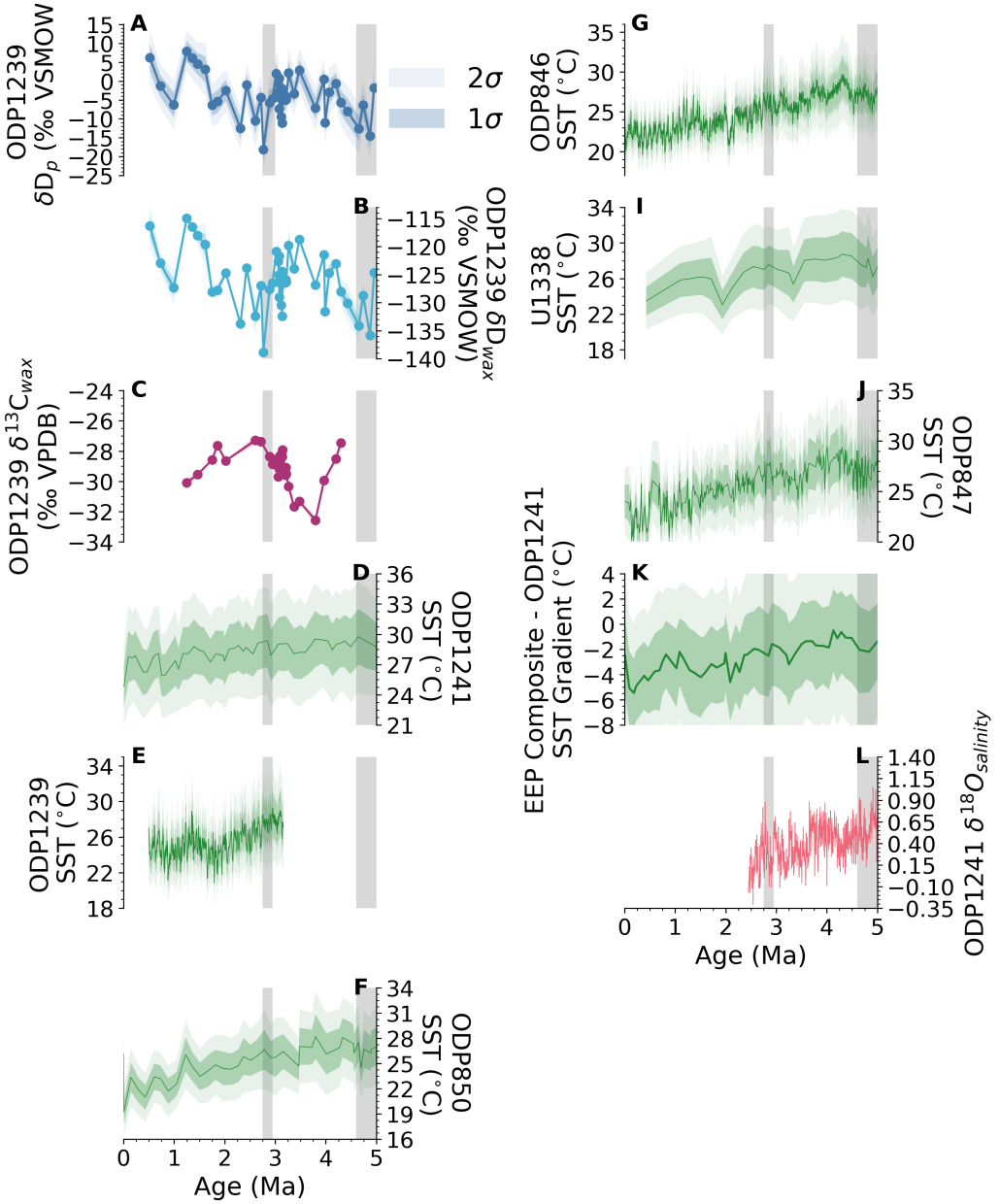

Figure S6: (A) Reconstructed δD_p at ODP1239 as shown in Figure 3A. (B) δD_{wax} and (C) $\delta^{13}C_{wax}$ of C_{30} *n*-alkanoic acids at ODP1239. (D-J) Reconstructed alkenone sea surface temperatures from ODP1241 (Seki et al., 2012), ODP1239 (Etourneau et al., 2010), ODP850 (Zhang et al., 2014b), ODP846 (Lawrence et al., 2006), IODP U1338 (Rousselle et al., 2013), and ODP847 (Dekens et al., 2007) calibrated using BAYSPLINE (Tierney and Tingley, 2018). (K) The sea surface temperature gradient between the cold tongue and off-equatorial (ODP1241) region of the eastern equatorial Pacific, as in Figure 3B. (L) $\delta^{18}O_{salinity}$ at ODP1239 as in Figure 3C. The shaded area corresponds to the early Pliocene (5.0 to 4.6 Ma) and the onset of major Northern Hemisphere glaciation (3.0 to 2.75 Ma).

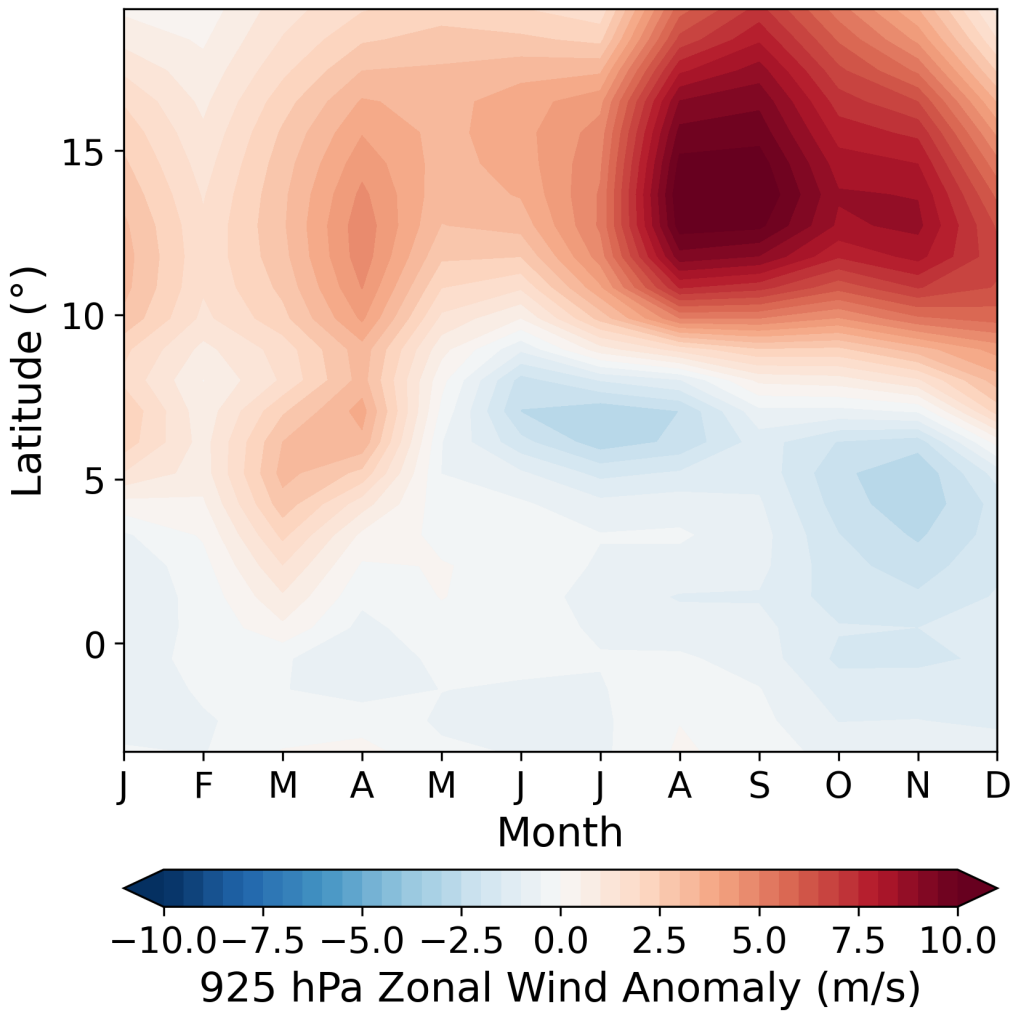

Figure S7: Hövmoller diagram of 925 hPa zonal wind anomalies (early Pliocene experiment - control) at 81 °W.

References

Aggarwal, P.K., Alduchov, O., Araguás Araguás, L., Dogramaci, S., Katzlberger, G., Kriz, K., Kulkarni, K.M., Kurttas, T., Newman, B.D., Purcher, A., 2007. New capabilities for studies using isotopes in the water cycle. Eos, Transactions American Geophysical Union 88, 537–538. doi:10.1029/2007EO490002.

Akaike, H., 1973. Information Theory and an Extension of the Maximum Likelihood Principle, in: Petrov, B.N., Csaki, F. (Eds.), Proceedings of the 2nd International Symposium on Information Theory. Akademiai Kiado, Budapest, pp. 267–281.

Ambach, W., Dansgaard, W., Eisner, H., Møller, J., 1968. The altitude effect on the isotopic composition of precipitation and glacier ice in the Alps. Tellus 20, 595–600. doi:10.1111/j.2153-3490.1968.tb00402.x.

Amundson, R., Dietrich, W., Bellugi, D., Ewing, S., Nishiizumi, K., Chong, G., Owen, J., Finkel, R., Heimsath, A., Stewart, B., Caffee, M., 2012. Geomorphologic evidence for the late Pliocene onset of hyperaridity in the Atacama Desert. GSA Bulletin 124, 1048–1070. doi:10.1130/B30445.1.

Barrett, B.S., Hameed, S., 2017. Seasonal Variability in Precipitation in Central and Southern Chile: Modulation by the South Pacific High. Journal of Climate 30, 55–69. doi:10.1175/JCLI-D-16-0019.1.

Bhattacharya, T., Feng, R., Tierney, J.E., Rubbelke, C., Burls, N., Knapp, S., Fu, M., 2022. Expansion and Intensification of the North American Monsoon During the Pliocene. AGU Advances 3, e2022AV000757. doi:10.1029/2022AV000757.

Bhattacharya, T., Tierney, J.E., Addison, J.A., Murray, J.W., 2018. Ice-sheet modulation of deglacial North American monsoon intensification. Nature Geoscience 11, 848–+. doi:10.1038/s41561-018-0220-7.

Bjerknes, J., 1969. Atmospheric teleconnections from the equatorial Pacific. Monthly Weather Review 97, 163–172. doi:10.1175/1520-0493(1969)097¡0163:ATFTEP¿2.3.CO;2.

Brady, E., Stevenson, S., Bailey, D., Liu, Z., Noone, D., Nusbaumer, J., Otto-Bliesner, B.L., Tabor, C., Tomas, R., Wong, T., Zhang, J., Zhu,

J., 2019. The Connected Isotopic Water Cycle in the Community Earth System Model Version 1. Journal of Advances in Modeling Earth Systems 11, 2547–2566. doi:10.1029/2019MS001663.

Broccoli, A.J., Dahl, K.A., Stouffer, R.J., 2006. Response of the ITCZ to Northern Hemisphere cooling. Geophysical Research Letters 33. doi:10.1029/2005gl024546.

Burls, N.J., Fedorov, A.V., 2014. Simulating Pliocene warmth and a permanent El Niño-like state: The role of cloud albedo. Paleoceanography 29, 893–910. doi:10.1002/2014PA002644.

Chiang, J.C.H., Biasutti, M., Battisti, D.S., 2003. Sensitivity of the Atlantic Intertropical Convergence Zone to Last Glacial Maximum boundary conditions. Paleoceanography 18. doi:Artn 1094 10.1029/2003pa000916.

Chiang, J.C.H., Bitz, C.M., 2005. Influence of high latitude ice cover on the marine Intertropical Convergence Zone. Climate Dynamics 25, 477–496. doi:10.1007/s00382-005-0040-5.

Dansgaard, W., 1964. Stable isotopes in precipitation. Tellus 16, 436–468.

Dee, S., Bailey, A., Conroy, J.L., Atwood, A., Stevenson, S., Nusbaumer, J., Noone, D., 2023. Water isotopes, climate variability, and the hydrological cycle: Recent advances and new frontiers. Environmental Research: Climate 2, 022002. doi:10.1088/2752-5295/accbe1.

Dekens, P.S., Ravelo, A.C., McCarthy, M.D., 2007. Warm upwelling regions in the Pliocene warm period. Paleoceanography 22. doi:10.1029/2006PA001394.

Echeverri, S., Cardona, A., Pardo, A., Monsalve, G., Valencia, V.A., Borrero, C., Rosero, S., López, S., 2015. Regional provenance from southwestern Colombia fore-arc and intra-arc basins: Implications for Middle to Late Miocene orogeny in the Northern Andes. Terra Nova 27, 356–363. doi:10.1111/ter.12167.

Eglinton, G., Hamilton, R.J., 1967. Leaf epicuticular waxes. Science 156, 1322–+. doi:10.1126/science.156.3780.1322.

Etourneau, J., Schneider, R., Blanz, T., Martinez, P., 2010. Intensification of the Walker and Hadley atmospheric circulations during the Pliocene–Pleistocene climate transition. Earth and Planetary Science Letters 297, 103–110. doi:10.1016/j.epsl.2010.06.010.

Fahad, A.A., Burls, N.J., Swenson, E.T., Straus, D.M., 2021. The Influence of South Pacific Convergence Zone Heating on the South Pacific Subtropical Anticyclone. Journal of Climate 34, 3787–3798. doi:10.1175/JCLI-D-20-0509.1.

Fastovich, D., Bhattacharya, T., Pérez-Ángel, L., Burls, N., Feng, R., Knapp, S., Mayer, T., 2023. Plio-Pleistocene evolution of westerly moisture transport into the northern tropical Andes. Zenodo. doi:10.5281/ZENODO.10301984.

Fedorov, A.V., Burls, N.J., Lawrence, K.T., Peterson, L.C., 2015. Tightly linked zonal and meridional sea surface temperature gradients over the past five million years. Nature Geoscience 8, 975–980. doi:10.1038/ngeo2577.

Fedorov, A.V., Dekens, P.S., McCarthy, M., Ravelo, A.C., deMenocal, P.B., Barreiro, M., Pacanowski, R.C., Philander, S.G., 2006. The Pliocene Paradox (Mechanisms for a Permanent El Niño). Science 312, 1485–1489. doi:10.1126/science.1122666.

Ford, H.L., Ravelo, A.C., Dekens, P.S., LaRiviere, J.P., Wara, M.W., 2015. The evolution of the equatorial thermocline and the early Pliocene El Padre mean state. Geophysical Research Letters 42, 4878–4887. doi:10.1002/2015GL064215.

Gao, L., Edwards, E.J., Zeng, Y., Huang, Y., 2014. Major Evolutionary Trends in Hydrogen Isotope Fractionation of Vascular Plant Leaf Waxes. PLOS ONE 9, e112610. doi:10.1371/journal.pone.0112610.

Garcia, M., Villalba, F., Araguas-Araguas, L., Rozanski, K., 1998. The Role of Atmospheric Circulation Patterns in Controlling the Regional Distribution of Stable Isotope Contents in Precipitation: Preliminary Results from Two Transects in the Ecuadorian Andes. IAEA, International Atomic Energy Agency (IAEA).

Garcia-Delgado, H., Petley, D.N., Bermúdez, M.A., Sepúlveda, S.A., 2022. Fatal landslides in Colombia (from historical times to 2020) and their

socio-economic impacts. Landslides 19, 1689–1716. doi:10.1007/s10346-022-01870-2.

Grimmer, F., Dupont, L., Lamy, F., Jung, G., González, C., Wefer, G., 2018. Early Pliocene vegetation and hydrology changes in western equatorial South America. Climate of the Past 14, 1739–1754. doi:10.5194/cp-14-1739-2018.

Grimmer, F., Dupont, L.M., Jung, G., Wefer, G., 2020. Piacenzian Environmental Change and the Onset of Cool and Dry Conditions in Tropical South America. Paleoceanography and Paleoclimatology 35, e2020PA004060. doi:10.1029/2020PA004060.

Groeneveld, J., 2005. Effect of the Pliocene Closure of the Panamanian Gateway on Caribbean and East Pacific Sea Surface Temperatures and Salinities by Applying Combined Mg/Ca and d18O Measurements (5.6 - 2.2 Ma). Ph.D. thesis.

Groeneveld, J., Hathorne, E.C., Steinke, S., DeBey, H., Mackensen, A., Tiedemann, R., 2014. Glacial induced closure of the Panamanian Gateway during Marine Isotope Stages (MIS) 95–100 (∼2.5 Ma). Earth and Planetary Science Letters 404, 296–306. doi:10.1016/j.epsl.2014.08.007.

Hartley, A.J., Chong, G., 2002. Late Pliocene age for the Atacama Desert: Implications for the desertification of western South America. Geology 30, 43–46. doi:10.1130/0091-7613(2002)030¡0043:LPAFTA¿2.0.CO;2.

Herbert, T.D., Lawrence, K.T., Tzanova, A., Peterson, L.C., Caballero-Gill, R., Kelly, C.S., 2016. Late Miocene global cooling and the rise of modern ecosystems. Nature Geoscience 9, 843–847. doi:10.1038/ngeo2813.

Hersbach, H., Bell, B., Berrisford, P., Hirahara, S., Horányi, A., Muñoz-Sabater, J., Nicolas, J., Peubey, C., Radu, R., Schepers, D., Simmons, A., Soci, C., Abdalla, S., Abellan, X., Balsamo, G., Bechtold, P., Biavati, G., Bidlot, J., Bonavita, M., De Chiara, G., Dahlgren, P., Dee, D., Diamantakis, M., Dragani, R., Flemming, J., Forbes, R., Fuentes, M., Geer, A., Haimberger, L., Healy, S., Hogan, R.J., Hólm, E., Janisková, M., Keeley, S., Laloyaux, P., Lopez, P., Lupu, C., Radnoti, G., de Rosnay, P., Rozum, I., Vamborg, F., Villaume, S., Thépaut, J.N., 2020. The ERA5

global reanalysis. Quarterly Journal of the Royal Meteorological Society 146, 1999–2049. doi:10.1002/qj.3803.

Heusser, L.E., Shackleton, N.J., 1994. Tropical Climatic Variation on the Pacific Slopes of the Ecuadorian Andes Based on a 25,000-Year Pollen Record from Deep-Sea Sediment Core Tri 163-31B. Quaternary Research 42, 222–225. doi:10.1006/qres.1994.1072.

Hovan, S.A., 1995. 28. Late Cenozoic atmospheric circulation intensity and climatic history recorded by Eolian deposition in the Eastern Equatorial Pacific Ocean, Leg 138. Proceedings of the Ocean Drilling Program, Scientific Results. Proceedings of the Ocean Drilling Program, Scientific Results , 615–625.

Hoyos, I., Cañón-Barriga, J., Arenas-Suárez, T., Dominguez, F., Rodríguez, B.A., 2019. Variability of regional atmospheric moisture over Northern South America: Patterns and underlying phenomena. Climate Dynamics 52, 893–911. doi:10.1007/s00382-018-4172-9.

Hoyos, I., Dominguez, F., Cañón-Barriga, J., Martínez, J.A., Nieto, R., Gimeno, L., Dirmeyer, P.A., 2018. Moisture origin and transport processes in Colombia, northern South America. Climate Dynamics 50, 971–990. doi:10.1007/s00382-017-3653-6.

Hu, J., Emile-Geay, J., Nusbaumer, J., Noone, D., 2018. Impact of Convective Activity on Precipitation δ18O in Isotope-Enabled General Circulation Models. Journal of Geophysical Research: Atmospheres 123, 13,595–13,610. doi:10.1029/2018JD029187.

Ishii, M., Shouji, A., Sugimoto, S., Matsumoto, T., 2005. Objective analyses of sea-surface temperature and marine meteorological variables for the 20th century using ICOADS and the Kobe Collection. International Journal of Climatology 25, 865–879. doi:10.1002/joc.1169.

Knapp, S., Burls, N., Dee, S., Feng, R., Feakins, S.J., Bhattacharya, T., 2022a. Data for article "A Pliocene precipitation isotope proxy-model comparison assessing the hydrological fingerprints of sea surface temperature gradients" doi:10.5281/ZENODO.6953979.

Knapp, S., Burls, N.J., Dee, S., Feng, R., Feakins, S.J., Bhattacharya, T., 2022b. A Pliocene Precipitation Isotope Proxy-Model Comparison Assessing the Hydrological Fingerprints of Sea Surface Temperature Gradients. Paleoceanography and Paleoclimatology 37, e2021PA004401. doi:10.1029/2021PA004401.

Kusch, S., Rethemeyer, J., Schefuß, E., Mollenhauer, G., 2010. Controls on the age of vascular plant biomarkers in Black Sea sediments. Geochimica et Cosmochimica Acta 74, 7031–7047. doi:10.1016/j.gca.2010.09.005.

Lawrence, K.T., Liu, Z., Herbert, T.D., 2006. Evolution of the Eastern Tropical Pacific Through Plio-Pleistocene Glaciation. Science 312, 79–83. doi:10.1126/science.1120395.

León, S., Cardona, A., Parra, M., Sobel, E.R., Jaramillo, J.S., Glodny, J., Valencia, V.A., Chew, D., Montes, C., Posada, G., Monsalve, G., Pardo-Trujillo, A., 2018. Transition From Collisional to Subduction-Related Regimes: An Example From Neogene Panama-Nazca-South America Interactions. Tectonics 37, 119–139. doi:10.1002/2017TC004785.

Lindzen, R.S., Nigam, S., 1987. On the Role of Sea Surface Temperature Gradients in Forcing Low-Level Winds and Convergence in the Tropics. Journal of the Atmospheric Sciences 44, 2418–2436. doi:10.1175/1520-0469(1987)044¡2418:OTROSS¿2.0.CO;2.

Lisiecki, L.E., Raymo, M.E., 2005. A Pliocene-Pleistocene stack of 57 globally distributed benthic delta O-18 records. Paleoceanography 20. doi:Artn Pa1003 10.1029/2004pa001071.

Liu, J., Tian, J., Liu, Z., Herbert, T.D., Fedorov, A.V., Lyle, M., 2019. Eastern equatorial Pacific cold tongue evolution since the late Miocene linked to extratropical climate. Science Advances 5, eaau6060. doi:10.1126/sciadv.aau6060.

Locarnini, R.A., Mishonov, A.V., Antonov, J.I., Boyer, T.P., Garcia, H.E., Baranova, O.K., Zweng, M.M., Paver, C.R., Reagan, J.R., Johnson, D.R., Hamilton, M., Seidov, 1948, D., Levitus, S., 2013. World ocean atlas 2013. Volume 1, Temperature doi:10.7289/V55X26VD.

Marchant, R., Almeida, L., Behling, H., Berrio, J.C., Bush, M., Cleef, A., Duivenvoorden, J., Kappelle, M., De Oliveira, P., Teixeira de Oliveira-Filho, A., Lozano-Garćia, S., Hooghiemstra, H., Ledru, M.P., Ludlow-Wiechers, B., Markgraf, V., Mancini, V., Paez, M., Prieto, A., Rangel, O., Salgado-Labouriau, M.L., 2002. Distribution and ecology of parent taxa of pollen lodged within the Latin American Pollen Database. Review of Palaeobotany and Palynology 121, 1–75. doi:10.1016/S0034-6667(02)00082-9.

Margirier, A., Strecker, M.R., Reiners, P.W., Thomson, S.N., Casado, I., George, S.W.M., Alvarado, A., 2023. Late Miocene Exhumation of the Western Cordillera, Ecuador, Driven by Increased Coupling Between the Subducting Carnegie Ridge and the South American Continent. Tectonics 42, e2022TC007344. doi:10.1029/2022TC007344.

Martínez, I., Keigwin, L., Barrows, T.T., Yokoyama, Y., Southon, J., 2003. La Niña-like conditions in the eastern equatorial Pacific and a stronger Choco jet in the northern Andes during the last glaciation. Paleoceanography 18. doi:10.1029/2002PA000877.

Martínez-Botí, M.A., Foster, G.L., Chalk, T.B., Rohling, E.J., Sexton, P.F., Lunt, D.J., Pancost, R.D., Badger, M.P.S., Schmidt, D.N., 2015. Plio-Pleistocene climate sensitivity evaluated using high-resolution CO2 records. Nature 518, 49–54. doi:10.1038/nature14145.

Meinicke, N., Reimi, M.A., Ravelo, A.C., Meckler, A.N., 2021. Coupled Mg/Ca and Clumped Isotope Measurements Indicate Lack of Substantial Mixed Layer Cooling in the Western Pacific Warm Pool During the Last ∼5 Million Years. Paleoceanography and Paleoclimatology 36, e2020PA004115. doi:10.1029/2020PA004115.

Mix, A., Tiedemann, R., Blum, P., et al. (Eds.), 2003. Proceedings of the Ocean Drilling Program, 202 Initial Reports. volume 202 of *Proceedings of the Ocean Drilling Program*. Ocean Drilling Program. doi:10.2973/odp.proc.ir.202.2003.

Morán-Tejeda, E., Bazo, J., López-Moreno, J.I., Aguilar, E., Azorín-Molina, C., Sanchez-Lorenzo, A., Martínez, R., Nieto, J.J., Mejía, R., Martín-Hernández, N., Vicente-Serrano, S.M., 2016. Climate trends and variability

in Ecuador (1966–2011). International Journal of Climatology 36, 3839–3855. doi:10.1002/joc.4597.

Myers, N., Mittermeier, R.A., Mittermeier, C.G., da Fonseca, G.A.B., Kent, J., 2000. Biodiversity hotspots for conservation priorities. Nature 403, 853–858. doi:10.1038/35002501.

Nakagawa, S., Schielzeth, H., 2013. A general and simple method for obtaining R2 from generalized linear mixed-effects models. Methods in Ecology and Evolution 4, 133–142. doi:10.1111/j.2041-210x.2012.00261.x.

O'Dea, A., Lessios, H.A., Coates, A.G., Eytan, R.I., Restrepo-Moreno, S.A., Cione, A.L., Collins, L.S., de Queiroz, A., Farris, D.W., Norris, R.D., Stallard, R.F., Woodburne, M.O., Aguilera, O., Aubry, M.P., Berggren, W.A., Budd, A.F., Cozzuol, M.A., Coppard, S.E., Duque-Caro, H., Finnegan, S., Gasparini, G.M., Grossman, E.L., Johnson, K.G., Keigwin, L.D., Knowlton, N., Leigh, E.G., Leonard-Pingel, J.S., Marko, P.B., Pyenson, N.D., Rachello-Dolmen, P.G., Soibelzon, E., Soibelzon, L., Todd, J.A., Vermeij, G.J., Jackson, J.B.C., 2016. Formation of the Isthmus of Panama. Science Advances 2, e1600883. doi:10.1126/sciadv.1600883.

Osorio-Granada, E., Restrepo-Moreno, S.A., Muñoz-Valencia, J.A., Trejos-Tamayo, R.A., Pardo-Trujillo, A., Barbosa-Espitia, A.A., 2017. Detrital zircon typology and U/Pb geochronology for the Miocene Ladrilleros-Juanchaco sedimentary sequence, Equatorial Pacific (Colombia): New constraints on provenance and paleogeography in northwestern South America. Geologica Acta: an international earth science journal 15, 201–215.

Pérez-Angel, L.C., Sepúlveda, J., Montes, C., Smith, J.J., Molnar, P., González-Arango, C., Snell, K.E., Dildar, N., 2022. Mixed Signals From the Stable Isotope Composition of Precipitation and Plant Waxes in the Northern Tropical Andes. Journal of Geophysical Research: Biogeosciences 127, e2022JG006932. doi:10.1029/2022JG006932.

Poveda, G., Jaramillo, L., Vallejo, L.F., 2014. Seasonal precipitation patterns along pathways of South American low-level jets and aerial rivers. Water Resources Research 50, 98–118. doi:10.1002/2013WR014087.

Poveda, G., Mesa, O.J., 2000. On the existence of Lloró (the rainiest locality on Earth): Enhanced ocean-land-atmosphere interaction by a low-level jet. Geophysical Research Letters 27, 1675–1678. doi:10.1029/1999GL006091.

Poveda, G., Waylen, P.R., Pulwarty, R.S., 2006. Annual and inter-annual variability of the present climate in northern South America and southern Mesoamerica. Palaeogeography, Palaeoclimatology, Palaeoecology 234, 3–27. doi:10.1016/j.palaeo.2005.10.031.

Quintana, J.M., Aceituno, P., 2012. Changes in the rainfall regime along the extratropical west coast of South America (Chile): 30-43º S. Atmósfera 25, 1–22.

Ramirez-Villegas, J., Salazar, M., Jarvis, A., Navarro-Racines, C.E., 2012. A way forward on adaptation to climate change in Colombian agriculture: Perspectives towards 2050. Climatic Change 115, 611–628. doi:10.1007/s10584-012-0500-y.

Rangel, T.F., Edwards, N.R., Holden, P.B., Diniz-Filho, J.A.F., Gosling, W.D., Coelho, M.T.P., Cassemiro, F.A.S., Rahbek, C., Colwell, R.K., 2018. Modeling the ecology and evolution of biodiversity: Biogeographical cradles, museums, and graves. Science doi:10.1126/science.aar5452.

Raymo, M.E., 1994. The initiation of Northern Hemisphere glaciation. Annual Review of Earth and Planetary Sciences 22, 353–383. doi:10.1146/annurev.ea.22.050194.002033.

Rincón-Martínez, D., Lamy, F., Contreras, S., Leduc, G., Bard, E., Saukel, C., Blanz, T., Mackensen, A., Tiedemann, R., 2010. More humid interglacials in Ecuador during the past 500 kyr linked to latitudinal shifts of the equatorial front and the Intertropical Convergence Zone in the eastern tropical Pacific. Paleoceanography 25. doi:10.1029/2009PA001868.

Rousselle, G., Beltran, C., Sicre, M.A., Raffi, I., De Rafélis, M., 2013. Changes in sea-surface conditions in the Equatorial Pacific during the middle Miocene–Pliocene as inferred from coccolith geochemistry. Earth and Planetary Science Letters 361, 412–421. doi:10.1016/j.epsl.2012.11.003.

Rowley, D.B., Garzione, C.N., 2007. Stable Isotope-Based Paleoaltimetry. Annual Review of Earth and Planetary Sciences 35, 463–508. doi:10.1146/annurev.earth.35.031306.140155.

Rozanski, K., Araguás-Araguás, L., Gonfiantini, R., 1993. Isotopic Patterns in Modern Global Precipitation, in: Climate Change in Conti-

nental Isotopic Records. American Geophysical Union (AGU), pp. 1–36. doi:10.1029/GM078p0001.

Sachse, D., Billault, I., Bowen, G.J., Chikaraishi, Y., Dawson, T.E., Feakins, S.J., Freeman, K.H., Magill, C.R., McInerney, F.A., van der Meer, M.T.J., Polissar, P., Robins, R.J., Sachs, J.P., Schmidt, H.L., Sessions, A.L., White, J.W.C., West, J.B., Kahmen, A., 2012. Molecular Paleohydrology: Interpreting the Hydrogen- Isotopic Composition of Lipid Biomarkers from Photosynthesizing Organisms, in: Jeanloz, R. (Ed.), Annual Review of Earth and Planetary Sciences, Vol 40. Annual Reviews, Palo Alto. volume 40 of *Annual Review of Earth and Planetary Sciences*, pp. 221–249.

Sakamoto, M.S., Ambrizzi, T., Poveda, G., 2011. Moisture Sources and Life Cycle of Convective Systems over Western Colombia. Advances in Meteorology 2011, e890759. doi:10.1155/2011/890759.

Salati, E., Dall'Olio, A., Matsui, E., Gat, J.R., 1979. Recycling of water in the Amazon Basin: An isotopic study. Water Resources Research 15, 1250–1258. doi:10.1029/WR015i005p01250.

Sauer, P.E., Eglinton, T.I., Hayes, J.M., Schimmelmann, A., Sessions, A.L., 2001. Compound-specific D/H ratios of lipid biomarkers from sediments as a proxy for environmental and climatic conditions. Geochimica et Cosmochimica Acta 65, 213–222. doi:10.1016/s0016-7037(00)00520-2.

Schneider, T., Bischoff, T., Haug, G.H., 2014. Migrations and dynamics of the intertropical convergence zone. Nature 513, 45–53. doi:10.1038/nature13636.

Schneider, U., Becker, A., Finger, P., Meyer-Christoffer, A., Rudolf, B., Ziese, M., 2011. GPCC full data reanalysis version 6.0 at 0.5: Monthly land-surface precipitation from rain-gauges built on GTS-based and historic data. GPCC Data Repository 10.

Seki, O., Schmidt, D.N., Schouten, S., Hopmans, E.C., Sinninghe Damsté, J.S., Pancost, R.D., 2012. Paleoceanographic changes in the Eastern Equatorial Pacific over the last 10 Myr. Paleoceanography 27. doi:10.1029/2011PA002158.

Sessions, A.L., Burgoyne, T.W., Schimmelmann, A., Hayes, J.M., 1999. Fractionation of hydrogen isotopes in lipid biosynthesis. Organic Geochemistry 30, 1193–1200. doi:10.1016/S0146-6380(99)00094-7.

Sierra, J.P., Arias, P.A., Durán-Quesada, A.M., Tapias, K.A., Vieira, S.C., Martínez, J.A., 2021. The Choco low-level jet: Past, present and future. Climate Dynamics 56, 2667–2692. doi:10.1007/s00382-020-05611-w.

Sierra, J.P., Arias, P.A., Vieira, S.C., 2015. Precipitation over Northern South America and Its Seasonal Variability as Simulated by the CMIP5 Models. Advances in Meteorology 2015, e634720. doi:10.1155/2015/634720.

Sierra, J.P., Arias, P.A., Vieira, S.C., Agudelo, J., 2018. How well do CMIP5 models simulate the low-level jet in western Colombia? Climate Dynamics 51, 2247–2265. doi:10.1007/s00382-017-4010-5.

Smith, F.A., Freeman, K.H., 2006. Influence of physiology and climate on δD of leaf wax n-alkanes from C3 and C4 grasses. Geochimica et Cosmochimica Acta 70, 1172–1187. doi:10.1016/j.gca.2005.11.006.

Spikings, R., Simpson, G., 2014. Rock uplift and exhumation of continental margins by the collision, accretion, and subduction of buoyant and topographically prominent oceanic crust. Tectonics 33, 635–655. doi:10.1002/2013TC003425.

Spikings, R.A., Crowhurst, P.V., Winkler, W., Villagomez, D., 2010. Syn- and post-accretionary cooling history of the Ecuadorian Andes constrained by their in-situ and detrital thermochronometric record. Journal of South American Earth Sciences 30, 121–133. doi:10.1016/j.jsames.2010.04.002.

Spikings, R.A., Winkler, W., Seward, D., Handler, R., 2001. Along-strike variations in the thermal and tectonic response of the continental Ecuadorian Andes to the collision with heterogeneous oceanic crust. Earth and Planetary Science Letters 186, 57–73. doi:10.1016/S0012-821X(01)00225-4.

Sternberg, L., 1988. D/H ratios of environmental water recorded by D/H ratios of plant lipids. Nature 333, 59–61. doi:10.1038/333059a0.

Strub, T., Mesias, J., Montecino, V., Rutllant, J., Salinas, S., 1998. Coastal ocean circulation off western South America, in: Robinson, A., Brink, K. (Eds.), The Sea, Volume 11: The Global Coastal Ocean: Regional Studies and Syntheses. Wiley, New York, pp. 273–315.

Tierney, J.E., Haywood, A.M., Feng, R., Bhattacharya, T., Otto-Bliesner, B.L., 2019. Pliocene Warmth Consistent With Greenhouse Gas Forcing. Geophysical Research Letters 46, 9136–9144. doi:10.1029/2019GL083802.

Tierney, J.E., Pausata, F.S.R., deMenocal, P.B., 2017. Rainfall regimes of the Green Sahara. Science Advances 3, e1601503. doi:10.1126/sciadv.1601503.

Tierney, J.E., Russell, J.M., 2007. Abrupt climate change in southeast tropical Africa influenced by Indian monsoon variability and ITCZ migration. Geophysical Research Letters 34. doi:10.1029/2007gl029508.

Tierney, J.E., Tingley, M.P., 2018. BAYSPLINE: A New Calibration for the Alkenone Paleothermometer. Paleoceanography and Paleoclimatology 33, 281–301. doi:10.1002/2017PA003201.

Timmermann, A., Lorenz, S.J., An, S.I., Clement, A., Xie, S.P., 2007. The Effect of Orbital Forcing on the Mean Climate and Variability of the Tropical Pacific. Journal of Climate 20, 4147–4159. doi:10.1175/JCLI4240.1.

Vicente-Serrano, S.M., Aguilar, E., Martínez, R., Martín-Hernández, N., Azorin-Molina, C., Sanchez-Lorenzo, A., El Kenawy, A., Tomás-Burguera, M., Moran-Tejeda, E., López-Moreno, J.I., Revuelto, J., Beguería, S., Nieto, J.J., Drumond, A., Gimeno, L., Nieto, R., 2017. The complex influence of ENSO on droughts in Ecuador. Climate Dynamics 48, 405–427. doi:10.1007/s00382-016-3082-y.

Villagómez, D., Spikings, R., 2013. Thermochronology and tectonics of the Central and Western Cordilleras of Colombia: Early Cretaceous–Tertiary evolution of the Northern Andes. Lithos 160–161, 228–249. doi:10.1016/j.lithos.2012.12.008.

Vuille, M., Francou, B., Wagnon, P., Juen, I., Kaser, G., Mark, B.G., Bradley, R.S., 2008. Climate change and tropical Andean glaciers: Past, present and future. Earth-Science Reviews 89, 79–96. doi:10.1016/j.earscirev.2008.04.002.

Wara, M.W., Ravelo, A.C., Delaney, M.L., 2005. Permanent El Niño-Like Conditions During the Pliocene Warm Period. Science 309, 758–761. doi:10.1126/science.1112596.

Waylen, P.R., Caviedes, C.N., 1986. El Niño and annual floods on the north Peruvian littoral. Journal of Hydrology 89, 141–156. doi:10.1016/0022-1694(86)90148-4.

White, S.M., Ravelo, A.C., 2020. The Benthic B/Ca Record at Site 806: New Constraints on the Temperature of the West Pacific Warm Pool and the "El Padre" State in the Pliocene. Paleoceanography and Paleoclimatology 35, e2019PA003812. doi:10.1029/2019PA003812.

Xie, S.P., Philander, S.G.H., 1994. A coupled ocean-atmosphere model of relevance to the ITCZ in the eastern Pacific. Tellus A 46, 340–350. doi:10.1034/j.1600-0870.1994.t01-1-00001.x.

Zhang, X., Lohmann, G., Knorr, G., Purcell, C., 2014a. Abrupt glacial climate shifts controlled by ice sheet changes. Nature 512, 290.

Zhang, Y.G., Pagani, M., Liu, Z., 2014b. A 12-Million-Year Temperature History of the Tropical Pacific Ocean. Science 344, 84–87. doi:10.1126/science.1246172.